Observational Evidence of Occurrence and Environmental Influences

DAVID C. FRITTS[©], ^{a,b} GERD BAUMGARTEN, ^c P.-DOMINIQUE PAUTET, ^d JAMES H. HECHT, ^e BIFFORD P. WILLIAMS, ^a NATALIE KAIFLER, ^f BERND KAIFLER, ^f C. BJORN KJELLSTRAND, ^g LING WANG, ^{a,b} MICHAEL J. TAYLOR, ^d AND AMBER D. MILLER ^h

^a GATS, Boulder, Colorado

b Center for Space and Atmospheric Research, Embry–Riddle Aeronautical University, Daytona Beach, Florida

c Leibniz Institute of Atmospheric Physics, University of Rostock, Kühlungsborn, Germany

d Department of Physics, Utah State University, Logan, Utah

c Space Science Applications Laboratory, The Aerospace Corporation, El Segundo, California

f German Aerospace Center, Oberpfaffenhofen, Germany

g School of Earth and Space Exploration, Arizona State University, Tempe, Arizona

h Department of Physics and Astronomy, University of Southern California, Los Angeles, California

(Manuscript received 31 August 2022, in final form 20 April 2023, accepted 24 April 2023)

ABSTRACT: Multiple recent observations in the mesosphere have revealed large-scale Kelvin–Helmholtz instabilities (KHI) exhibiting diverse spatial features and temporal evolutions. The first event reported by Hecht et al. exhibited multiple features resembling those seen to arise in early laboratory shear-flow studies described as "tube" and "knot" (T&K) dynamics by Thorpe. The potential importance of T&K dynamics in the atmosphere, and in the oceans and other stratified and sheared fluids, is due to their accelerated turbulence transitions and elevated energy dissipation rates relative to KHI turbulence transitions occurring in their absence. Motivated by these studies, we survey recent observational evidence of multiscale Kelvin–Helmholtz instabilities throughout the atmosphere, many features of which closely resemble T&K dynamics observed in the laboratory and idealized initial modeling. These efforts will guide further modeling assessing the potential importance of these T&K dynamics in turbulence generation, energy dissipation, and mixing throughout the atmosphere and other fluids. We expect these dynamics to have implications for parameterizing mixing and transport in stratified shear flows in the atmosphere and oceans that have not been considered to date. Companion papers describe results of a multiscale gravity wave direct numerical simulation (DNS) that serendipitously exhibits a number of KHI T&K events and an idealized multiscale DNS of KHI T&K dynamics without gravity wave influences.

SIGNIFICANCE STATEMENT: Kelvin–Helmholtz instabilities (KHI) occur throughout the atmosphere and induce turbulence and mixing that need to be represented in weather prediction and other models of the atmosphere and oceans. This paper documents recent atmospheric evidence for widespread, more intense, features of KHI dynamics that arise where KH billows are initially discontinuous, misaligned, or varying along their axes. These features initiate strong local vortex interactions described as "tubes" and "knots" in early laboratory experiments, suggested by, but not recognized in, earlier atmospheric and oceanic profiling, and only recently confirmed in newer, high-resolution atmospheric imaging and idealized modeling to date.

KEYWORDS: Kelvin-Helmholtz instabilities; Stability; Small scale processes; Remote sensing

1. Introduction

All models employed to describe atmospheric dynamics in regional, mesoscale, or global domains are unable to resolve flow instabilities leading to turbulence, mixing, and transport, hence must rely on parameterizations of these dynamics and

Openotes content that is immediately available upon publication as open access.

© Supplemental information related to this paper is available at the Journals Online website: https://doi.org/10.1175/JAS-D-22-0189.s1.

Corresponding author: David C. Fritts, dave@gats-inc.com

their influences at unresolved scales. In stably stratified environments from the stable boundary layer (SBL) into the mesosphere and lower thermosphere (MLT), the major contributors at smaller scales are gravity wave (GW) breaking and Kelvin–Helmholtz instabilities (KHI) including "tube" and "knot" (T&K) dynamics or variants of these dynamics in multiscale (MS) environments such as described by Fritts et al. (2013, hereafter F13), Fritts and Wang (2013, hereafter FW13), and Fritts et al. (2016, hereafter F16).

Importantly, current parameterizations are very crude, and fail in key areas to account for the relevant dynamics. As examples, most "whole atmosphere" models employ GW parameterizations that account for constraints on GW amplitudes, but "tune" the mixing influences (effectively the turbulence Prandtl number, Pr) to achieve the desired mean fields (Garcia et al. 2014). Such models typically ignore coincident, but distinct, KHI dynamics driving mixing of strongly stratified layers that are in

DOI: 10.1175/JAS-D-22-0189.1

most or all cases unresolved, but which may imply significant local mixing and transport (see F13 and FW13). This is especially true in the SBL (Fernando and Weil 2010; Baklanov et al. 2011), where the major contributing dynamics remain to be explored, modeled, and characterized.

This is likely also the case throughout the atmosphere, due to the inability of current parameterizations in global models to account for sufficient mixing and transport in the MLT (e.g., Garcia et al. 2014; Liu 2021). A long series of in situ tracer measurements has revealed persistent, intense shears accompanying large-amplitude inertia-GWs (IGWs) at altitudes of ~90–130 km (Larsen 2002) and local, large-scale KHI (Mesquita et al. 2020), neither of which are described realistically in local or global models. Significant shears and IGWs having vertical wavelengths $\lambda_z \sim 1$ km or smaller are ubiquitous in radiosonde profiles in the troposphere and stratosphere, imply major missing shear variances, but are not described in regional or global models due to the inability to characterize their horizontal wavelengths λ_h and orientations because of insufficient spatial and temporal sampling. The implications of increasing large-scale KHI, $\lambda_h \sim 3-15$ km, from the troposphere into the MLT, and for enhanced turbulence and mixing due to KHI T&K dynamics, remain to be assessed, and may be key missing components of current parameterizations.

Quantitative observations of KHI in the atmosphere began ~70 years ago and have provided key insights into their diverse dynamics in varying environments up to the present. Early observations of thin tropospheric clouds revealed KHI spatial scales and variable axial coherence at these altitudes (Scorer 1951, 1969; Scorer and Wexler 1963; Ludlam 1967). Related early quantitative observations including stereo imaging of often very thin noctilucent clouds when viewed from the ground (Witt 1962), and referred to more generally as polar mesospheric clouds (PMCs) hereafter, occur at altitudes of ~83 km (Schäfer et al. 2020) in polar summer. These revealed KHI spatial scales, variable axial coherence, and evolutions in the presence of large-amplitude GWs. Early studies in the oceans revealed similar KHI dynamics and apparent GW influences (e.g., Woods 1968; Woods and Wiley 1972).

These various observations motivated multiple laboratory shear flow studies that revealed fine details of KH billows and emerging smaller-scale features via shadowgraph techniques by Thorpe (1973a,b, 1985, 1987), Schowalter et al. (1994), Caulfield et al. (1996), Holt (1998), and others. The laboratory studies enabled detailed descriptions of various instabilities driving KHI billow transitions to turbulence, including 1) streamwisealigned counterrotating convective instabilities (CI) in the outer regions of the KH billows, 2) secondary, smaller-scale KHI arising in the stratified braids between adjacent KH billows, and 3) additional features Thorpe described as "tubes and knots." The T&K features seen in multiple laboratory experiments were observed to have various forms, to arise where KH billows were initially misaligned or exhibited phase variations along their axes, and to initiate much more rapid transitions to turbulence than accompanying CI or secondary KHI of individual KH billows.

Subsequent atmospheric studies employing aircraft in situ measurements, radar and lidar profiling, and improved OH

airglow and PMC imaging in the mesosphere revealed KHI to exhibit a wide range of dynamics, scales, and variability from the SBL into the thermosphere (e.g., Browning and Watkins 1970; Fritts and Rastogi 1985; Gossard 1990; Eaton et al. 1995; De Silva et al. 1996; Blumen et al. 2001; Hecht et al. 2005, 2014, hereafter H14; Luce et al. 2007, 2008, 2018; Hysell et al. 2012; Baumgarten and Fritts 2014, hereafter BF14; Fritts et al. 2014; hereafter F14). A number of these studies revealed additional evidence of interacting KH billows and likely T&K dynamics, but this was not their primary focus, nor noted at the time.

Observations of tropospheric clouds were revisited by Thorpe (2002), who inferred typical ratios of KH billow coherence lengths to billow wavelengths of \sim 3–8 km, suggested that these features arise due to GW influences, and noted apparent examples of misaligned and merging KH billows suggestive of T&K dynamics. High-resolution radar profiling in the SBL and residual layer by Eaton et al. (1995) exhibited significant spatial variability in small-scale KHI suggesting nonuniform billows and likely T&K dynamics. Similar radar profiling in the troposphere and lower stratosphere by Luce et al. (2007, 2008, 2018) revealed MS KHI spatial variations suggesting likely T&K dynamics at larger scales. More recent radar volumetric imaging by Chau et al. (2020) captured a KHI event revealing apparent irregular KH billows having wavelengths of $\lambda_h \sim 5$ –8 km centered at ~85 km in the mesosphere also suggestive of T&K dynamics. Related ocean profiling of KHI yielded similar evidence of irregular billow amplitudes and λ_h again suggestive of T&K dynamics (Moum et al. 2003; Geyer et al. 2010; Chang et al. 2016; Tu et al. 2020).

Improved ground-based imaging of PMCs provided more compelling evidence for modulation of KHI by the underlying GW fields (BF14; F14), while the new Aerospace Corporation Near-IR Imager (ANI) yielded KHI observations at several sites (Hecht et al. 2018, 2005; H14). The latter of these revealed larger-scale KHI exhibiting varying coherence lengths, billow core undulations, and smaller-scale secondary instabilities, but no specific evidence of small-scale KHI T&K dynamics was identified in these observations.

Further improved abilities to quantify small-scale dynamics in the mesosphere were provided by a new Aerospace Corporation Near-IR OH Imager (ANI2) employing higher resolution than ANI in a smaller field of view (FOV), \sim 22 m and \sim 47 km, respectively. Common ANI and ANI2 observations obtained at the Andes Lidar Observatory (ALO) in 2016 captured a dramatic KHI T&K event accompanying KH billow $\lambda_h \sim$ 7–10 km that revealed a broad suite of T&K dynamics and CI of individual KH billows. These were described by Hecht et al. (2021, hereafter H21) and motivated initial modeling of KHI T&K dynamics by Fritts et al. (2021, hereafter F21).

Similar capabilities were provided by subsequent PMC imaging aboard the PMC Turbo stratospheric balloon that flew in July 2018 at an altitude of \sim 37 km and hosted four wide and three narrow FOV PMC imagers. These imagers enabled resolution of features at spatial scales as small as \sim 40–80 m enabling identification of additional instability features characterizing T&K dynamics due to interactions among KH billows having wavelengths of $\lambda_h \sim 5$ km that were misaligned or exhibited

TABLE 1. Abbreviations employed in the text.

Abbreviation	Expansion	Abbreviation	Expansion
ALO	Andes Lidar Observatory	FW23	Fritts and Wang (2023)
AMTM	Advanced Mesosphere Temperature Mapper	GW	Gravity wave
ANI	Aerospace Corporation Near-IR Imager	H14	Hecht et al. (2014)
ANI2	Advanced Aerospace Corp. Near-IR Imager	H21	Hecht et al. (2021)
BF14	Baumgarten and Fritts (2014)	IGW	Inertia-GW
BOLIDE	Balloon Lidar Experiment	KHI	Kelvin-Helmholtz instability
CI	Convective instabilities	K22	Kjellstrand et al. (2022)
CORAL	Compact Rayleigh Autonomous Lidar	MLT	Mesosphere and lower thermosphere
DLR	German Aerospace Center	MS	Multiscale
DNS	Direct numerical simulation	N-S	North-south
EBEX	E and B Experiment	OH	OH molecule
F13	Fritts et al. (2013)	PFRR	Poker Flat Research Range
F14	Fritts et al. (2014)	PMCs	Polar mesospheric cloud(s)
F16	Fritts et al. (2016)	Pr	Prandtl number
F19	Fritts et al. (2019)	Re	Reynolds number
F21	Fritts et al. (2021)	Ri	Richardson number
F22a	Fritts et al. (2022a)	SBL	Stable boundary layer
F22b	Fritts et al. (2022b)	SRWTL	Na Wind-Temperature Lidar
F22c	Fritts et al. (2022c)	TDF	Tierra del Fuego, Argentina
F23	Fritts et al. (2023)	T&K	Tube and knot
FMCW	Full width at half maximum	UT	Universal time
FOV	Field of view	2D	Two-dimensional
FW13	Fritts and Wang (2013)	3D	Three-dimensional

variable phases along their axes (Kjellstrand et al. 2022, hereafter K22).

Our objectives in this paper are to explore the evidence for KHI T&K dynamics, and their environments, in the MLT. While evidence of KHI T&K dynamics reviewed above reveals them to occur throughout the atmosphere, the MLT offers several clear advantages:

- KHI λ_h ~ 5–10 km or larger enable T&K dynamics at spatial scales able to be resolved over large regions by current ground-based and recent balloon-borne observations,
- imaging of relatively thin PMC and OH airglow layers enables identification of KHI T&K dynamics and evolutions and also captures the scales, orientations, and evolutions of the GW fields in which they arise, and
- vertical profiling capabilities by lidars and radars frequently reveal KHI, and apparent T&K modulations, and are occasionally coincident with imaging.

An example of KHI T&K features occurring in an idealized direct numerical simulation (DNS) described in the companion paper by Fritts et al. (2023, manuscript submitted to *J. Atmos. Sci.*, hereafter F23) are shown for reference in section 2. Imaging and profiling capabilities enabling quantification of KHI T&K events, environments, and scales are reviewed in section 3. Observational evidence of KHI T&K dynamics, environments, and evolutions revealed in imaging and profiling of the MLT PMC and OH airglow layers are discussed in sections 4 and 5. Implications of these observations and their relations to previous studies of MLT dynamics are discussed in section 6, and our conclusions are presented in section 7. A list of abbreviations is provided in Table 1.

2. DNS guidance of KHI T&K dynamics identification

KHI T&K dynamics can be very diverse, as their tendency to emerge surely depends on multiple factors, some of which are known, but also others that remain to be explored. The initial laboratory shear flow studies by Thorpe (1985, 1987) revealed 1) a "tube" identified as a link between adjacent KH billows comprising a single vortex emerging on the intermediate vortex sheet and wrapping over and under the adjacent KH billows and 2) a "knot" identified as a link where two KH billows connect to a single billow along their axes where they were initially misaligned [see the imaging and cartoons of these dynamics in Thorpe (1987)].

A further linkage among adjacent KH billows is billow pairing seen to occur occasionally in the laboratory by Thorpe (1987). These dynamics were described initially by Fritts (1984) in a small two-dimensional (2D) domain for small Reynolds and Richardson numbers, Re = 100 and Ri = 0.05. KH billow pairing also occurs at larger Re, but can be precluded by more rapidly emerging, smaller-scale instabilities (Mashayek and Peltier 2013). Billow pairing also occurs in response to random initial conditions for weak random noise, and in the absence of larger-scale perturbations of the initial shear layer, as described below.

We illustrate in Fig. 1 the range of KHI T&K dynamics identified to date with three-dimensional (3D) imaging of an MS KHI event viewed from above and described in detail by F23. The quantity displayed is the negative eigenvalue, λ_2 , of the tensor defined as $\mathbf{H} = \mathbf{S}^2 + \mathbf{R}^2$, where \mathbf{S} and \mathbf{R} are the strain and rotation tensors (Jeong and Hussain 1995; Fritts et al. 2022a, hereafter F22a). Thus, λ_2 enables identification of features that exhibit rotational rather than shearing vorticity.

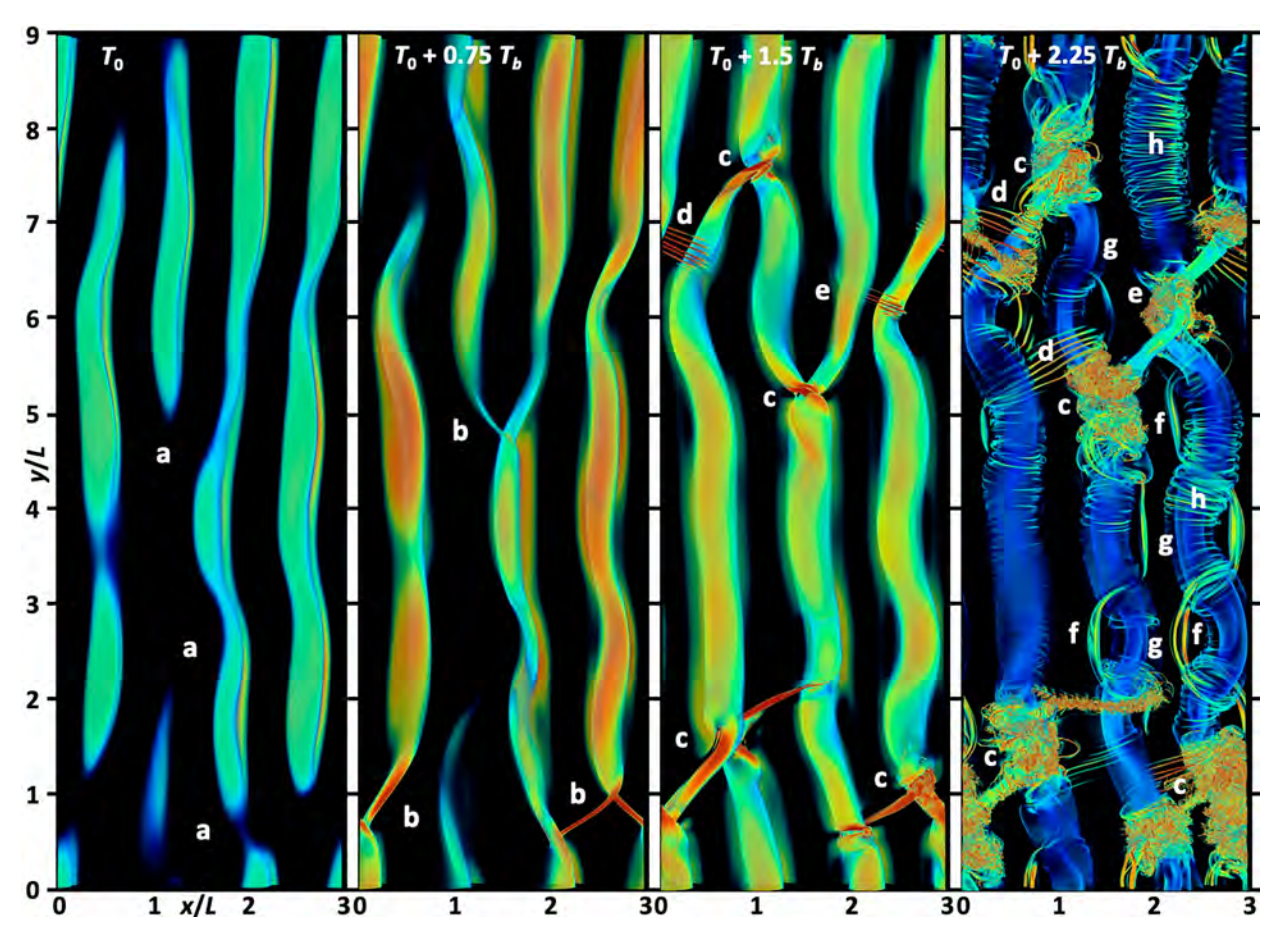


FIG. 1. Three-dimensional imaging of an MS KHI event revealed in λ_2 viewed from above and described in detail by F23. See text for details and F23 for comparisons with other Re.

The DNS was performed for Re = 3000, less than the maximum Re = 5000 described by F23, in order to reveal the major features of the KHI T&K evolution prior to the breakdown of CI that arise quickly within the outer KH billow cores. The computational domain was specified to enable significant KH billow phase variations along their axes (along y) and either three or four KH billows to emerge along the wind shear (along x) in the periodic domain. The imaging is shown at a cadence of $0.75T_b$, for buoyancy period $T_b = 2\pi/N = 222$ s at the peak buoyancy frequency N = 0.0283 s⁻¹ at the maximum shear, thus spans an interval of \sim 8.3 min.

The λ_2 evolution reveals the following features arising from the weak initial noise seed:

- 1) weak, discontinuous initial KH billows emerge having three or four wavelengths along *x*, and somewhat variable phases along *y* (sites a in Fig. 1),
- 2) intensifying KH billows and differential stretching of the vortex sheets occur where KH billows are misaligned along *y* and initiate vortex "tubes" (sites b),
- 3) sites where 2 KH billows link to 1, or where a vortex tube links adjacent KH billows, yield initial vortex "knots" that drive rapid transitions to strong turbulence (sites c),

- additional, smaller-scale vortex tubes emerge where adjacent KH billows exhibit significant phase variations along y (sites d),
- 5) a limited region where 2 billows arise in close proximity along *x* leads to local billow pairing that also drives rapid transitions to strong turbulence (site e),
- 6) increasing KH billow phase variations along y, due to differential vertical advection in z, cause stretching and intensification of the intermediate vortex sheets that enable secondary KHI to emerge at small scales (sites f),
- strong mutual advection of adjacent, roughly orthogonal, KH billow cores induce large-scale Kelvin vortex waves that exhibit strong helical oscillations we will refer to as Kelvin "twist waves" hereafter (Thomson 1880; Arendt and Fritts 1998) (sites g), and
- secondary CI in KH billows arise following initial turbulence transitions (sites h).

All features labeled b–g in Fig. 1 can be considered T&K dynamics, as they all arise due to misaligned initial KH billows, and they all precede secondary CI breakdown of individual KH billows.

3. Imaging and profiling capabilities

a. Imaging instruments

1) PMC IMAGING

PMC imaging has been performed from the ground for over 60 years. The more recent PMC imaging discussed here was performed with commercial digital cameras enabling automated operations over long intervals. That described by BF14 and F14 was performed with a Canon EOS 50D with a 135 mm f/2 lens yielding a FOV of $9.5^{\circ} \times 6.3^{\circ}$.

Serendipitous PMC imaging was obtained by star trackers aboard the NASA Astrophysics E and B Experiment (EBEX) on a stratospheric balloon flying over Antarctica at ~ 35 km for 11 days in austral summer 2012/13. These revealed stunning and diverse small-scale instability dynamics due to GW breaking and KHI seen at $\sim 2-5$ m resolution in a ~ 4 km $\times 4$ km FOV at a range of ~ 60 km.

EBEX PMC imaging motivated the NASA PMC Turbo experiment (Fritts et al. 2019, hereafter F19) hosting 7 pressure vessels each housing a high-resolution camera, a 50 or 135 mm lens, a control computer, and large data storage (Kjellstrand et al. 2020). Pixel binning (4×4) reduced noise and data storage and yielded ~ 20 –40 m resolution for routine analyses.

2) OH AIRGLOW IMAGING

OH airglow imaging employed here was performed by a variety of instruments. ANI and ANI2 at the ALO achieve moderate and very high spatial and temporal resolution, respectively, by employing H-band filters that allow the bright OH Meinel band at \sim 1550–1700 nm to be detected, thus enabling a pixel signal-to-noise ratio > 100:1. ANI (ANI2) employs a 256 × 256 (2048 × 2048) pixel detector and a custom lens providing a $73^{\circ} \times 73^{\circ}$ (29.6° × 29.6°) FOV yielding an ~100 km × 100 km (47 km \times 47 km) imaging area with pixel resolution of \sim 400 (22) m at \sim 89 km. The ANI2 images employed here used 2 \times 2 pixel binning yielding ~45 m superpixels. As employed by H14, H21, and the Advanced Mesosphere Temperature Mappers (AMTM) imaging employed in this study, difference imaging, using a Δt of ~20–60 s, was employed in the ANI and ANI2 analyses to enhance sensitivity to small-scale KHI T&K dynamics. Additional details on ANI and ANI2 are provided by H14 and H21.

AMTMs developed by USU (Pautet et al. 2014; Taylor et al. 2019) are operating, or have operated, at nine sites, two of which are employed in this study. These measure two OH Meinel (3, 1) band (1500–1550 nm) line intensities and a background channel that together enable a temperature measurement in each pixel, hence T(x, y) maps at a \sim 30-s cadence centered at the OH layer, typically at \sim 85–90 km, spanning a \sim 200 km \times 160 km field of view centered on zenith. Difference imaging at a $\Delta t \sim$ 35 s was employed to reveal the smaller-scale KHI T&K dynamics by removing more slowly varying features.

b. Profiling instruments

1) RAYLEIGH LIDAR

Rayleigh lidars developed by the German Aerospace Center (DLR) were employed both on the PMC Turbo payload, e.g.,

the Balloon Lidar Experiment (BOLIDE; Kaifler et al. 2020), and for long-term ground-based observations by the Compact Rayleigh Autonomous Lidar (CORAL; Kaifler and Kaifler 2021) in the MLT instrument cluster at Rio Grande on Tierra del Fuego (TdF), Argentina (53.8°S, 67.8°W). Both lidars provided continuous profiling of PMC brightness (where seen) spanning the PMC layer and atmospheric densities allowing T(z) profiles at lower altitudes (e.g., Kaifler et al. 2018; Reichert et al. 2021).

2) NA RESONANCE LIDAR

The Sodium Resonance Wind–Temperature Lidar (SRWTL) installed at Poker Flat Research Range (PFRR) in Alaska in 2017 (Li et al. 2020) is based on the former Na lidar operated at the Arctic Lidar Observatory for Middle Atmosphere Research from 2000 to 2017 (She et al. 2002; Williams et al. 2004, 2006) with a new solid-state laser seeding pulse dye amplifier. SRWTL is a narrowband lidar that cycles between 3 frequencies to measure the Doppler shift and thermal broadening of the Na back-scatter from $\sim\!\!80$ to 105 km. The $\sim\!\!1$ W beam is split into three beams pointing zenith and 20° north and east with telescopes fiber coupled to three receivers. Na density, temperature, and radial wind are measured continuously in each beam.

4. KHI T&K dynamics revealed in PMC imaging and profiling

The initial identification of KHI T&K dynamics over ALO by H21 confirmed Thorpe's (2002) suggestion that these dynamics should be prevalent in the atmosphere. Indeed, earlier observations reviewed above revealed multiple aspects of T&K dynamics, especially modulations of KHI events by GWs and distortions of billow cores by adjacent billows suggestive of emerging T&K dynamics, but these features were not described as such in those studies. Subsequent imaging at higher altitudes confirmed these features, but neither showed direct T&K links among billows nor identified them as KHI T&K dynamics (e.g., BF14; F14; F19; H14). H21 and K22 were the first observational studies to reveal direct T&K links between adjacent KH billows. Here we review earlier and more recent PMC imaging and profiling, and related lidar vertical profiling, for further evidence of these T&K dynamics, and their environments and prevalence, in the MLT.

a. PMC imaging

Two very different KHI events seen in high-resolution PMC imaging from Trondheim, Norway, on 1 August 2009 and from Kühlungsborn, Germany, on 24 June 2009 were analyzed and described by BF14 and F14 and exhibit a number of features relevant to this study. PMC imaging in Figs. 2a and 2b extends ~200 km horizontally at its center and shows an evolving large field of KHI exhibiting clear GW perturbations over a 10-min interval. Seen in Fig. 2b are large-scale, brighter bands aligned roughly upper left to lower right suggesting likely GW influences on KHI evolution. The 10-min interval reveals a rapid expansion of large amplitude KHI to the east and north, implying a significant and/or increasing shear, and decreasing Ri, at these times. Zoomed high-resolution imaging in the dashed rectangle in Fig. 2a spanning a 7-min interval in Figs. 2c-j

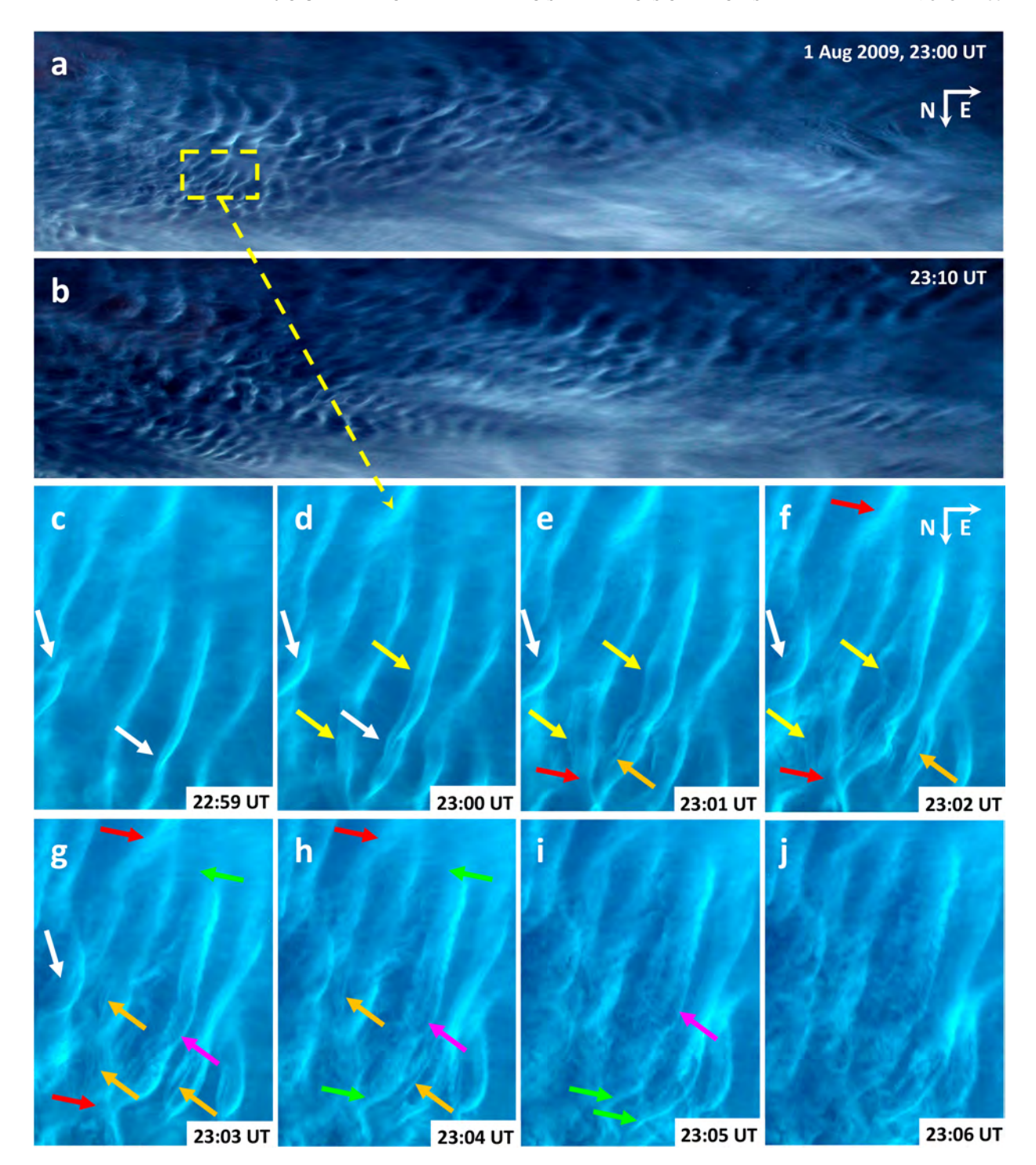


FIG. 2. PMC imaging from Trondheim, Norway, on 1 Aug 2009. (c)–(j) Arrows denote key features described in the text.

shows a sequence of KH billows having $\lambda_h \sim$ 3–5 km, with the images stretched north–south (N–S) to approximate viewing from below.

The imaging in Figs. 2c-j reveals KH billows exhibiting a diversity of features and evolutions we now recognize as T&K dynamics. These include the following:

- misaligned initial billow cores lead to a billow pairing event (left center) and large-scale twist waves (white arrows),
- the billow cores expand and fragment thereafter due to large-scale twist waves propagating away from their knot source dynamics (yellow arrows, toward the lower right),

- as seen to arise adjacent to sites c and seen at large amplitudes at sites g in Fig. 1,
- thin secondary KHI arise on the thin vortex sheets over, under, or between, and having vorticity aligned largely along, the billow cores (orange arrows, toward the upper left),
- 4) several billow cores exhibit CI aligned roughly orthogonally (pink arrows), as seen at sites h in Fig. 1,
- larger and smaller vortex tubes link adjacent KH billows, with the most pronounced occurring where the initial KH billows are more deformed (green arrows), and
- misaligned initial KH billows where one links to two (red arrows).

Regions where KH billows are misaligned or link via large-scale vortex tubes exhibit the most rapid breakdowns to less coherent structures and turbulence beginning at ~2300–2303 UT and progress to smaller scales rapidly thereafter. Importantly for our purposes, the collective influences of the initial KHI T&K dynamics induce increasing distortions of the billow cores seen below to be widespread in the MLT. All of these features are seen in the initial high-resolution modeling of KHI T&K dynamics (F21; F22a; Fritts et al. 2022b,c, hereafter F22b, F22c) and span a comparable interval as seen in the last three panels of Fig. 1. The online supplemental P1.Fig2.mp4 provides an animation of these dynamics.

PMC imaging obtained from northern Germany on 24 June 2009 projected to geophysical coordinates, as if viewed from above, and spanning only 4 min, is shown in Fig. 3 (see Figs. 1 and 2 in BF14). These panels show GW modulations of PMC brightness due to tilting of the PMC layer relative to the line of sight. This interval shows the emergence of small-scale KHI T&K dynamics where divergent horizontal GW motions intensify strongly stratified vortex sheets [see Fritts and Wang (2023, hereafter FW23) for details of these dynamics in a DNS of an MS GW flow]. As seen in Figs. 2c-j and discussed above, the small-scale KHI seen at left and right at the earlier times in Figs. 3a and 3b exhibit intensifying T&K distortions over this interval, and similar features are seen in the lee of other GW crests farther north in Fig. 3c. Of note, however, are the alignments of the emerging, small-scale T&K dynamics that are more nearly along than normal to the dominant GW propagation direction. This suggests a transverse component to the enhanced shear on the vorticity sheet relative to the GW propagation. P1.Fig3.mp4 provides an animation of these dynamics.

b. PMC imaging and profiling

Further insights into KHI T&K dynamics accompanied PMC imaging by the NASA PMC Turbo long-duration balloon flight at ~37 km from Esrange, Sweden, to northeast Canada in July 2018 (see F19). The key instruments included seven high-resolution imagers and the BOLIDE lidar. PMC imaging captured a wide diversity of dynamics events, among them multiple examples of larger- and smaller-scale KHI evolutions, the majority of which exhibited T&K dynamics. Two examples are illustrated in the first and second rows in Fig. 4.

T&K dynamics seen in Figs. 4a-c, described in detail by K22, reveal an extensive KHI display with KH billow $\lambda_h \sim 5$ km, strong GW modulations of billow coherence, and large KH billow distortions and misalignments along their axes. The evolution tracked with the black oval in Figs. 4a-c spans only 4 min, but exhibits major intensification of the KH billows, clear secondary KHI and CI of individual billows, and T&K dynamics driving rapid KH billow breakdown. Yellow (red) arrows show KH billows without (exhibiting) T&K dynamics. This PMC imaging confirms characterization of these same dynamics first observed over ALO by H21 (see the black oval tracking advection of a region exhibiting several such billow misalignments; yellow and red arrows highlight KH billows that are aligned and misaligned, for reference). P1.Fig4.mp4 provides an animation of the T&K dynamics in Figs. 4a-c.

Other PMC Turbo projected, two-camera image subsets in Figs. 4d and 4e suggest GW modulations of smaller-scale, $\lambda_h \sim 1$ km, KH billow coherence and emerging, but weaker, T&K dynamics necessarily having a much smaller Re. As noted in the above discussion of ground-based PMC observations, these PMC Turbo observations suggest that KHI T&K dynamics, and implied turbulence and mixing, are more widespread, and perhaps ubiquitous, than previously understood.

PMC imaging in Figs. 4f–i shows 4 examples of high-resolution imaging by the NASA EBEX experiment [see section 3a(1)]. The remarkable EBEX resolution and often thin PMCs enabled definition of features as small as the turbulence inner scale $l_0 \sim 50$ m for a kinematic viscosity $\nu \sim 1$ m² s⁻¹ and a typical $\varepsilon \sim 0.001$ W kg⁻¹ at \sim 82 km in polar summer (Rapp et al. 2004).

EBEX images in Figs. 4f and 4g spaced by \sim 1.5 min reveal what appear to be intensifying KHI exhibiting misaligned billows having $\lambda_h \sim 700$ m, and apparent secondary CI in the billow cores at center and lower left. Seen at center to lower right is an apparent intermediate, weaker billow that is initially discontinuous and begins to merge via T&K dynamics with the billow below. Importantly, an alternative explanation invoking propagating GWs is very unlikely in highly structured environments at small Re, and cannot account for the observed smaller-scale features. Likewise, ducted GWs that can occur at small scales in highly structured environments do not exhibit interactions among adjacent phases or small-scale instabilities.

The EBEX image in Fig. 4h suggests a KH billow core that is kinked by T&K interactions, with less distinct features at either side. It also exhibits multiple, orthogonal vortex tubes arising on the vortex sheet wrapping behind it, as seen in the PMC Turbo KHI images in Figs. 5b and 5c; also see FW23. The EBEX image in Fig. 4i suggests clear KHI and interactions among adjacent, and misaligned, KH billows having $\lambda_h \sim 50$ –200 m that must have very small Re and exhibit only weak, laminar interactions among adjacent billows. These features can only be viscous, small-scale KHI on a vortex sheet because counterrotating vortices cannot link via merging along their axes. Rather, they link via vortex loop formation in early stages of GW breaking (Andreassen et al. 1998; Fritts et al. 2009), in outer KH billows

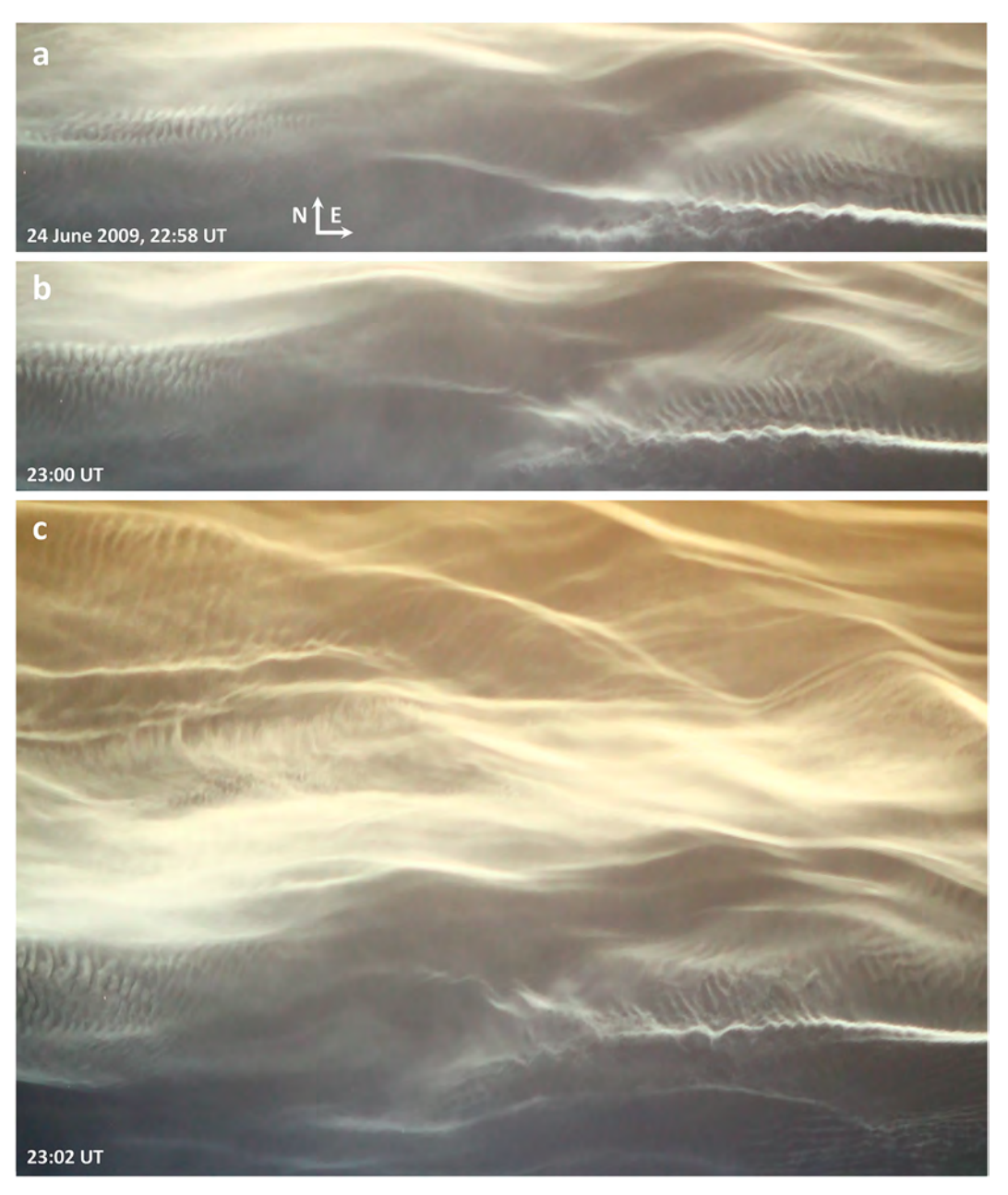


FIG. 3. PMC imaging over Scandinavia from Kühlungsborn, Germany, on 24 Jun 2009. See text for details.

where secondary CI intensify and link in local spanwise shear (F21; F22a; F22b), as "hairpin" vortices at late stages of shear flow restratification (Watanabe et al. 2019), and related dynamics with similar vortex alignments.

Vertical profiling of the PMC layer shown in Fig. 4j was performed by CORAL at Rio Grande on TdF. These observations were not accompanied by PMC imaging at TdF, which began more recently, but they clearly demonstrate the occurrence of MS KHI exhibiting T&K dynamics. Specific evidence includes 1) overturning features at their upper edges, 2) apparent periods of \sim 1–5 min implying variable λ_h , likely as large as \sim 5 km or

larger, based on maximum KH billow depths of \sim 1.5–2 km and an assumption of an initial Ri \sim 0.1–0.15 (Thorpe 1973b), and 3) a limited event duration of \sim 30 min. This event is also strikingly similar in character to other atmospheric and oceanic KHI profiling revealing these T&K dynamics noted above.

5. KHI T&K dynamics revealed in OH imaging and Na lidar profiling

OH imaging provides sensitivity to more diverse environments than PMC imaging via measurements spanning a wide

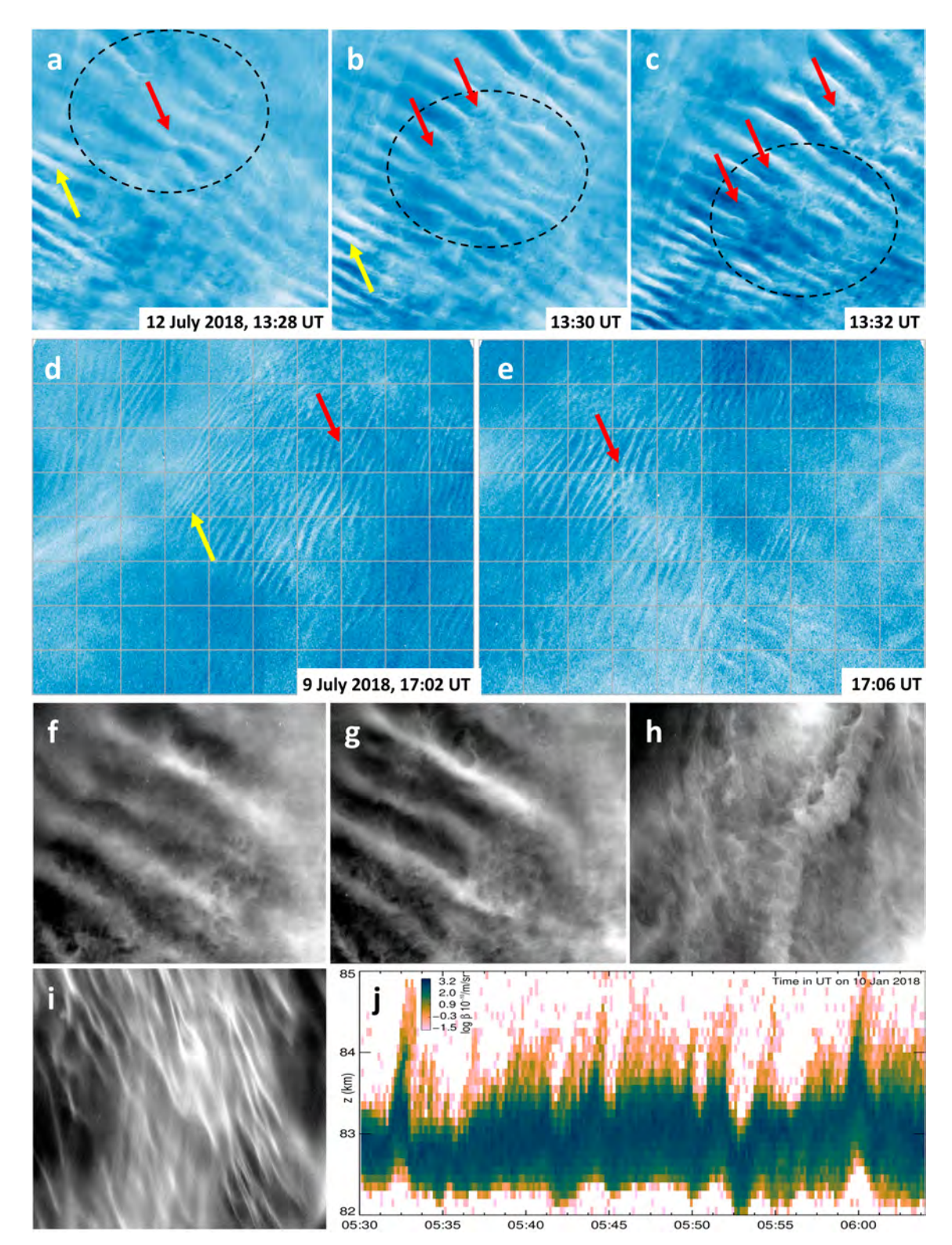


FIG. 4. (a)–(e) PMC Turbo imaging on 12 Jul 2018, (f)–(i) EBEX PMC imaging in December 2012–January 2013, and (j) PMC profiling by CORAL over TdF on 10 Jan 2018. The dashed oval and arrows in (a)–(e) track the central event advection and highlight key features (see text for details).

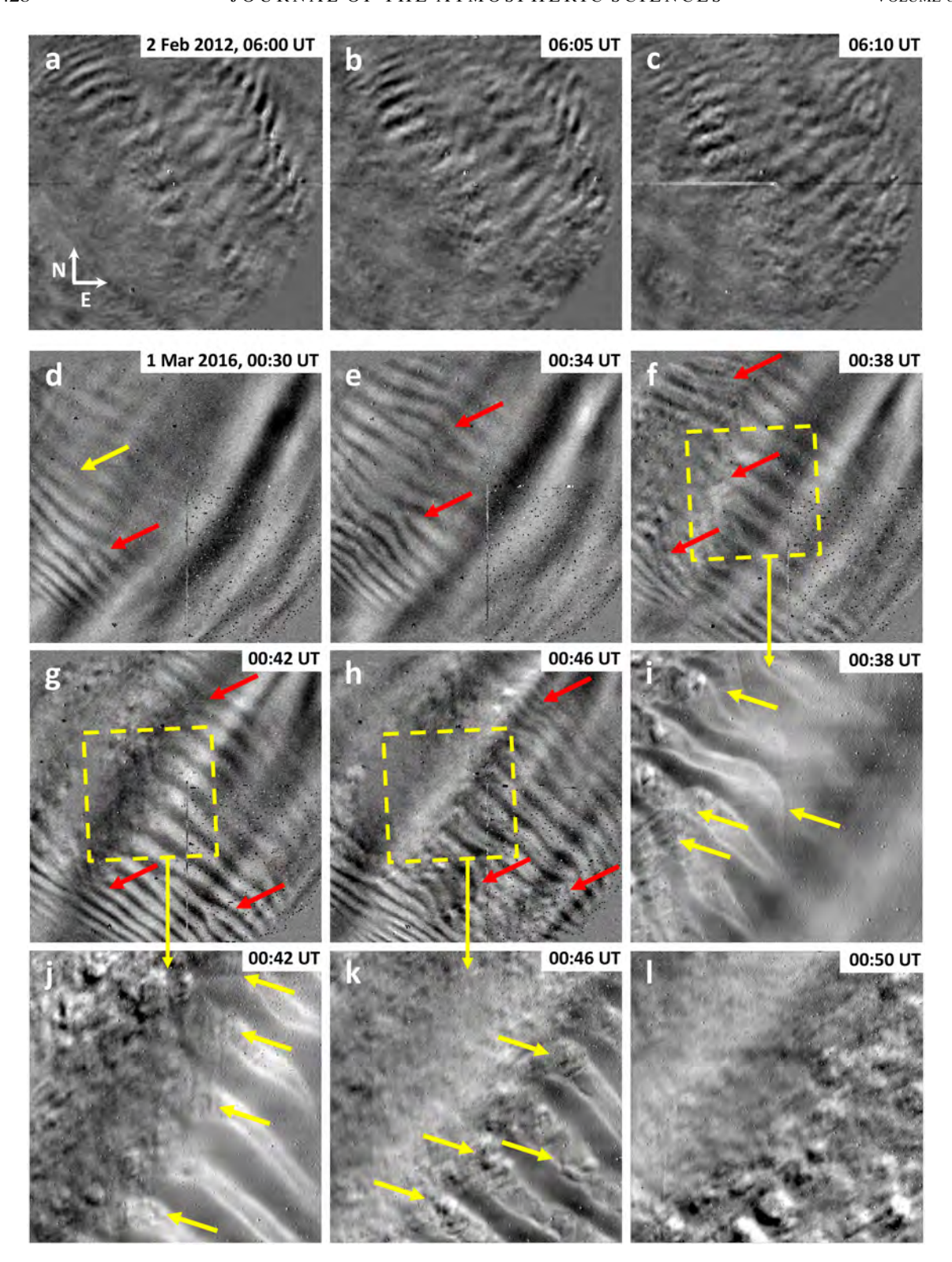


Fig. 5. ANI and ANI2 OH airglow difference imaging over ALO (a)–(c) on 2 Feb 2012 and (d)–(l) on 1 Mar 2016. See text for details.

range of MLT environments that vary with latitude, longitude, and season. Vertical viewing also removes potential ambiguities in interpretations of features seen in PMC imaging at low elevation angles where GW vertical displacements may be significant. This enables exploration of KHI responses 1) in MLT GW fields arising from diverse sources, 2) at common sites for varying MLT environments, and 3) potentially exhibiting systematic variations in latitude and season. OH imaging does not achieve the very high spatial resolution enabled by PMC imaging that captures dynamics driving, or within, the inertial range of turbulence. However, OH "difference" imaging at a specified Δt reveals instability features at small scales that advect or evolve over short intervals by eliminating the larger-scale, more slowly varying, mean, and GW contributions to OH brightness. This procedure is employed to explore T&K responses to varying MLT dynamics observed at multiple sites and reveals these dynamics to occur in a wide range of MLT environments. For consistency in our discussion, all OH fields are shown as if viewed from above.

Na lidar profiling of Na densities enables direct tracking of vertical displacements due to GWs and KHI, apart from small influences of vertical displacements over ~ 1 km or less and faster Na chemistry at the bottom edge of the Na layer on measured Na densities.

a. OH airglow imaging over ALO, Chile

ANI OH imaging over ALO by H14 revealed clear, large-scale ($\lambda_h \sim 8$ km) KHI exhibiting varying responses over 45 min. H14 noted varying KHI amplitudes on larger scales, varying phases along their axes, and smaller-scale, roughly orthogonal, apparent secondary instabilities emerging at later times. A review of these dynamics illustrated in Figs. 5a–c reveals a number of features that appear to be responses to T&K dynamics based on insights from initial MS modeling described by FW23. These include the following:

- KH billows arise in bands roughly normal to their axes likely due to GW modulations,
- 2) nearly uniform initial KH billow alignments become increasingly variable in time,
- emerging smaller-scale features induce links between adjacent billows, and
- 4) rapid billow breakdown occurs in regions exhibiting misalignments and linking.

The latter three of these T&K dynamics are seen to arise in the idealized DNS in Fig. 1.

More dramatic and quantitative imaging of the H21 ALO event using the wider FOV ANI is shown at larger scales in Figs. 5d-h. These images reveal more clearly GW influences on emerging T&K dynamics for KH billows having $\lambda_h \sim 7$ –10 km aligned largely along the GW propagation direction from lower right to upper left in these images. In this case, KH billows having small initial amplitudes and relatively uniform initial phases (Fig. 5d, yellow arrow) are seen to exhibit increasing phase distortions, phase kinking, and billow breakdown accompanying successive GW bright phases advancing

toward upper left as the KHI evolve toward lower right (see the red arrows in Figs. 5d-h).

Additional high-resolution $\sim 50 \text{ km} \times 50 \text{ km}$ ANI2 imaging indicated by the yellow rectangles in Figs. 5f-h from 0038 to 0050 UT are shown in Figs. 5i-l. These reveal the final stages of KHI T&K breakdown discussed by H21 and the further breakdown accompanying the successive GW bright phases impacting KHI having $\lambda_h \sim 7$ -10 km and exhibiting additional misaligned KH billows, vortex tubes, secondary instabilities, and their breakdown thereafter (see the regions indicated by yellow arrows in these fields).

The KHI T&K dynamics in this case were estimated by H21 to yield an energy dissipation rate as large as $\varepsilon \sim 1~\rm W~kg^{-1}$, which is consistent with those assessed using the DNS of KHI T&K dynamics by F22b scaled to the ALO KHI λ_h , and which is larger than that assessed by F22b in regions largely without T&K influences by \sim 2-4 times. P1.Fig5a.mov, P1.Fig5b.mp4, and P1.Fig5c.mp4 show these events in ANI and ANI2 imaging over longer intervals.

b. OH airglow imaging over Lauder, New Zealand

OH imaging by an AMTM in the lee of the southern Alps during the 2014 DEEPWAVE ground-based and airborne measurement program captured a diversity of mountain wave (MW), propagating GW, and instability responses, the majority of which also exhibited apparent KHI T&K dynamics. Two of these are illustrated in the upper and lower panels of Fig. 6. The first event observed on 31 May exhibits a bore passage with KHI T&K dynamics preceding and following the bore (Figs. 6a-c), but having roughly orthogonal orientations in these regions, and a strong decrease in T (red to blue in Figs. 6d-f) accompanying bore passage. A likely explanation for these differing responses is an increase of the OH layer altitude accompanying bore passage in an altered IGW or tidal environment having a rotary shear in altitude. These observations suggest that KHI T&K dynamics readily occur in environments exhibiting varying shear orientations in altitude. P1.Fig6a1.mp4 and P1.Fig6a2.mp4 show earlier and later stages of this event using AMTM difference imaging.

A second event observed over Lauder on 22 June (Figs. 6g–o) exhibits a remarkably chaotic field comprising MS KHI extending from \sim 1500 UT to beyond 1700 UT, and apparently accompanying strong MS GW shear orientations. Different KHI events and λ_h are seen in close proximity and apparently overlap in the same regions multiple times at different altitudes. This is expected for a single IGW (Lelong and Dunkerton 1998), and is surely the case for superposed IGWs. The absence of detectable GWs in the AMTM T(x, y) on 22 June implies relatively small GW λ_z , given the typical OH layer full width at half maximum (FWHM) of \sim 7 km, and/or GW $\lambda_h \sim$ 200 km or larger, consistent with an IGW environment.

KHI λ_h as large as \sim 10–15 km over Lauder are comparable to, or larger than, the largest KHI $\lambda_h \sim$ 10 km reported in previous MLT imaging and profiling studies (e.g., Hysell et al. 2012; Chau et al. 2020; Mesquita et al. 2020; H21). They also require strong shears having half widths of $h \sim \lambda_h/4\pi \sim 1.2$ km or larger, and a vector wind shear $d\mathbf{U}/dz \sim N/\mathrm{Ri}^{1/2}$, for Ri = $N^2h^2/|\mathbf{U}|^2 \sim 0.1$ to achieve a KH billow depth-to- λ_h ratio ~ 0.4 (Thorpe 1973b). These estimates imply $|\mathbf{U}| \sim 70 \mathrm{\ ms}^{-1}$ for a superposition

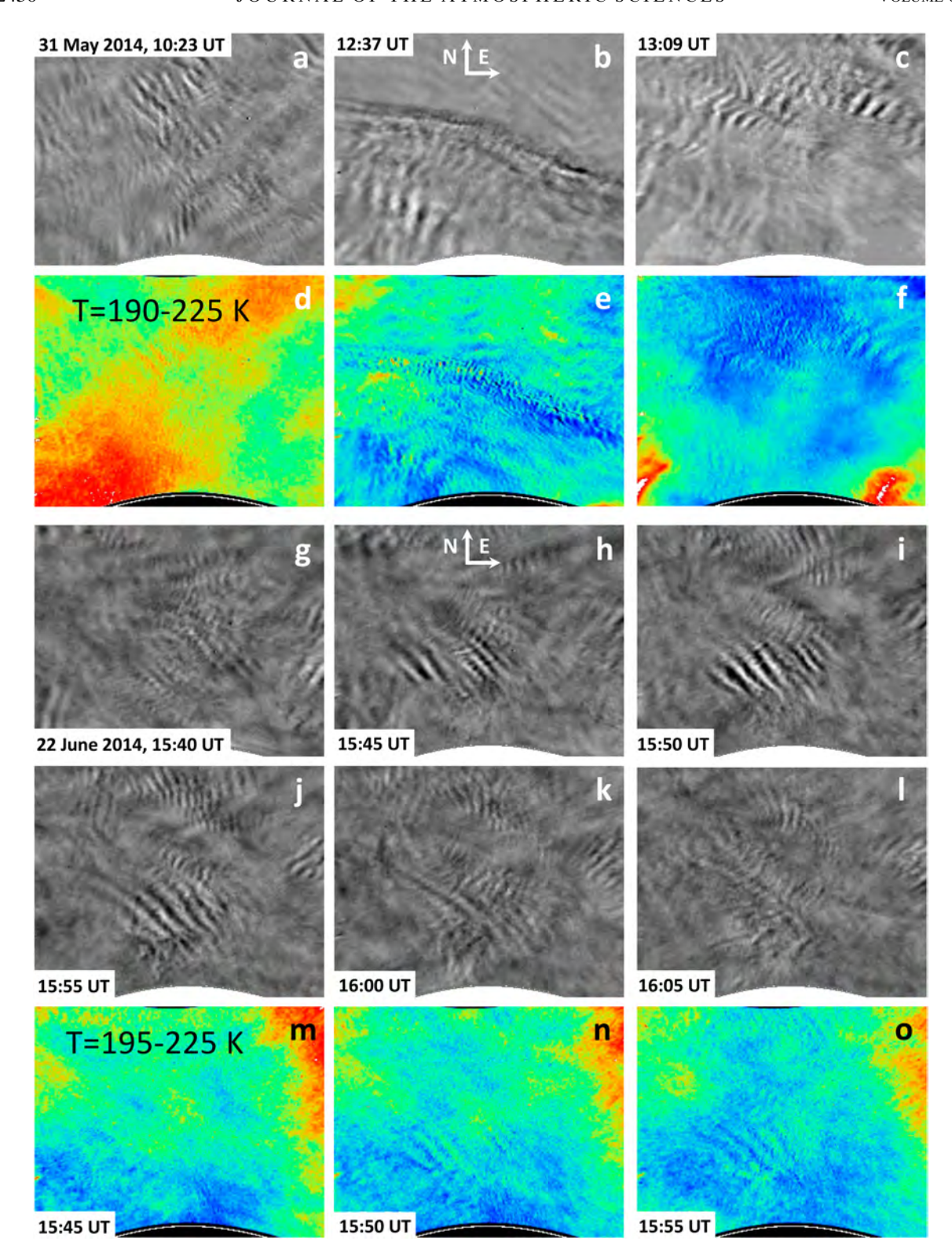


FIG. 6. AMTM OH (a)–(c),(g)–(l) airglow difference and (d)–(f),(m)–(o) temperature imaging over Lauder, New Zealand, on (a)–(f) 31 May and (g)– (o) 22 Jun 2014. Temperature ranges are shown in (d) and (m); see text for details.

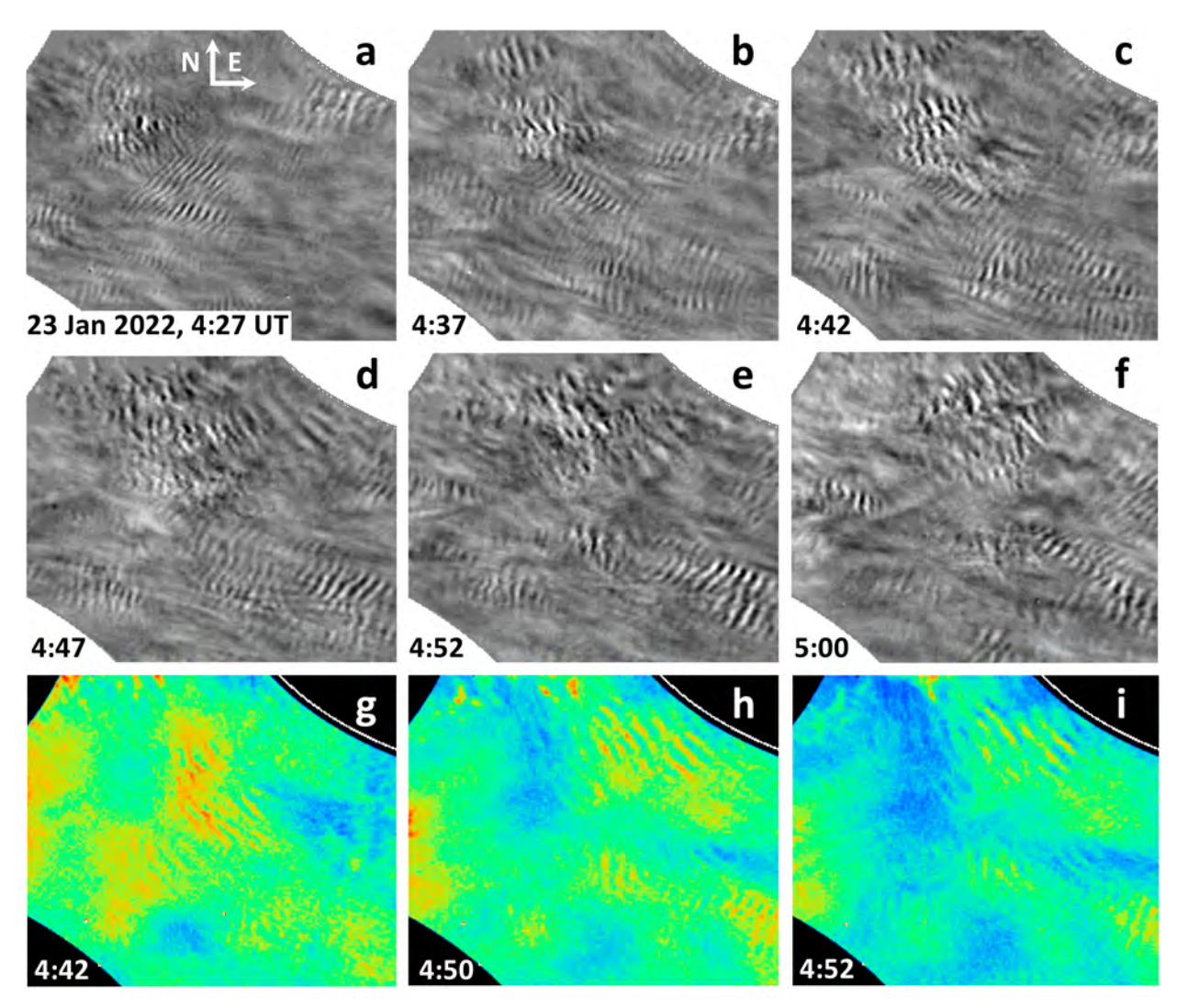


FIG. 7. As in Fig. 6, but over TdF on 23 Jan 2022. AMTM (a)-(f) difference and (g)-(i) temperature imaging. See text for details.

of IGWs because tidal λ_z are too large to account for the observed KHI λ_h . However, tidal shears likely contributed to local intensification of IGW shears due to IGW critical level approach, but not in defining the KHI λ_h , especially at smaller KHI scales.

A number of these Lauder KHI events, especially at the larger λ_h , also exhibit apparent transient, orthogonal vortex tubes that closely resemble those shown in the PMC image in Fig. 4h. These dynamics are complex, and P1.b.mp4 shows this sequence to include multiple, sometimes overlapping, evolutions exhibiting KHI formation, intensification, T&K dynamics, and subsequent KH billow fragmentation at multiple scales, orientations, and adjacent altitudes. The significance of such events, and their dependence on KHI scales, are discussed in section 6.

c. OH airglow imaging over TdF, Argentina

AMTM OH brightness difference and T(x, y) imaging over TdF on 23 January 2022 spanning 33 and 10 min, respectively, are shown in Fig. 7. As seen over Lauder, difference imaging at

TdF exhibits a wide diversity of apparent KHI responses at various scales in different regions over a short interval. In this case, there are fewer apparent overlaps of KHI responses having different scales and orientations at apparently different altitudes in the same regions. There are, however, multiple apparent KHI events in different regions at different times, exhibiting differing KHI λ_h and orientations, and overlapping in some cases (see the upper-left and right portions of Figs. 8a-d). The larger-scale events also have signatures in T(x, y) imaging. All the KHI events that can be followed over ~10-15 min exhibit T&K dynamics revealing increasing interactions, kinking, and breakdown along their axes with time. These KHI provide additional evidence to that shown in previous figures that such dynamics are widespread, and potentially ubiquitous where enhanced shear layers arise in MS GW fields, and which may make major contributions to mixing and transport where they arise.

An alternative explanation of small-scale bands seen in MLT airglow for many years is as ducted GWs having typical

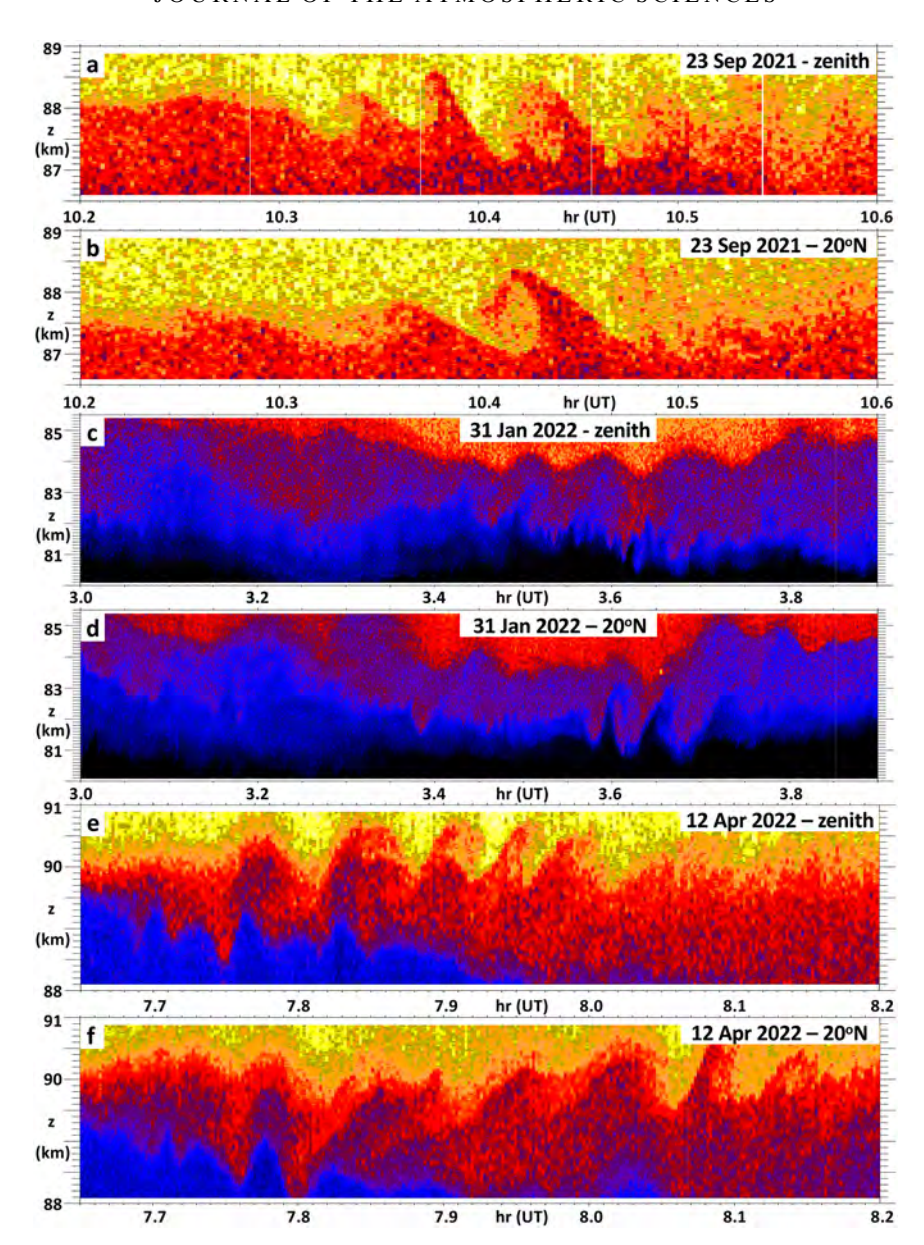


FIG. 8. Na lidar Na density profiling over PFRR, Alaska, on (a),(b) 23 Sep 2021, (c),(d) 31 Jan 2022, and (e),(f) 12 Apr 2022 at 8-s and 90 m resolution. See text for details.

 $\lambda_h \sim 10$ –20 km. These often exhibit varying, or misaligned, phases due to superposed packets. Importantly, however, such ducted GWs do not exhibit increasing phase kinking, nor linking via orthogonal vortices because they are largely linear, small-amplitude motions, there are no intensified vortex sheets, nor subsequent instabilities causing breakdown. P1.Fig7a.mp4 and P1.Fig7b.mp4 show the evolutions of the OH brightness difference and T(x,y) imaging over a longer interval for this KHI event.

d. Lidar profiling over the PFRR, Alaska

Lidar profiling of Na densities at the upper and lower edges of the Na layer centered at \sim 85–90 km has revealed large-scale KH billows at various sites (e.g., Pfrommer et al. 2009). Such

profiling at the upper edge of the Na layer represents vertical displacements quite accurately because Na chemistry is slow at these altitudes, though air parcel expansion causes small underestimates in vertical displacements inferred from Na densities. At the bottom edge of the Na layer, however, downward excursions are also underestimated due to much faster Na chemistry, both of which contribute to somewhat reduced apparent KH billow amplitudes.

Na lidar profiling yields many examples of KHI having varying billow amplitudes and λ_h as shear layers advect through the lidar beams, and as inferred in the PMC lidar profiling shown in Fig. 5j. Examples of such responses in three KHI events observed with the Na lidar at PFRR are shown in Fig. 8.

That in Figs. 8a and 8b obtained on 23 September 2021 exhibits strongly varying forms, amplitudes, and likely adjacent billow interactions among successive billows at the upper edge of the Na layer at two locations separated by \sim 30 km. The initial Ri is not known, but a representative Ri \sim 0.1 implies KHI $\lambda_h \sim$ 4–5 km (Thorpe 1973b). An Ri \sim 0.2 or larger implies larger, shallower KHI for which there is no apparent evidence.

Similar Na lidar profiling in zenith and 20°N beams on 31 January 2022 shown in Figs. 8c and 8d exhibit clear, largerscale, vertical displacements of the shear layer and significant variability in adjacent KH billows at each site and between the two beams. The descending shear layer is seen to be earlier and stronger in the zenith beam, and there are large differences in the subsequent KHI responses. Those in the zenith beam are more uniform and increase in amplitude prior to apparent billow breakdown after ~3.6 UT. Those in the lidar beam at 20°N reveal an initial, large KH billow displacement at ~3.4 UT, an apparent absence of KH billows for one or two cycles, and strongly increasing KH billow altitude extents approaching 3-4 km thereafter that may be a result of T&K dynamics or adjacent billow pairing. Billow advection is seen in both beams, but the varying apparent periods indicate differing KHI λ_h and/or orientations at these sites. The billow depths in this event for an assumed Ri ~ 0.1 imply KHI $\lambda_h \sim 3-5$ km in the zenith beam and perhaps larger in the beam at 20°N at later times, as seen in the AMTM imaging at several sites discussed above.

A third case over PFRR observed on 12 April 2022 in the zenith and 20°N beams shown in Figs. 8e and 8f exhibits KH billows having strongly varying forms and λ_h at both sites. The zenith beam appears to capture larger-scale billows with intermediate structures yielding smaller vertical displacements that suggest intermediate vortex tubes and emerging T&K dynamics. The KH billows seen in the 20°N beam reveals a billow train exhibiting apparent strong shearing and breakdown, though the lidar cannot resolve the details nor the temporal evolution. These and other PFRR lidar observations confirm the occurrence, character, and scales of KHI T&K dynamics inferred in OH and PMC imaging at altitudes of \sim 83–90 km.

6. Summary and discussion

Imaging and profiling observations described above reveal KHI dynamics to be widespread in the MLT, and to exhibit T&K dynamics at resolved scales. These results were not specifically selected for these purposes. In fact, we are not aware of any MLT imaging that clearly reveal KH billows having $\lambda_h \sim 5-15$ km that do not exhibit T&K dynamics, even in cases where GWs do not clearly contribute to modulating the local shear environments. The event shown in Fig. 2 having KHI $\lambda_h \sim 5$ km was recognized by F14 to exhibit billow-scale twist waves, but these were not attributed to T&K dynamics at that time. The events shown in Figs. 4a-c also having KHI $\lambda_h \sim 5$ km and those in Figs. 5d-i having KHI $\lambda_h \sim 7$ -10 km were the first to be described in terms of KHI T&K dynamics with supporting modeling (H21; F21, F22a,b,c; K22). The remaining 13 events and images have not been described previously.

The KHI events shown in PMCs in Figs. 3, 4d, and 4e having KH billow $\lambda_h \sim 1$ km exhibit clear, though less intense, T&K dynamics, despite likely quite small Re for small shear depths and scales and a kinematic, or weakly turbulent, viscosity $\nu \sim 1~{\rm m^2~s^{-1}}$ at the PMC layer. KHI T&K dynamics also occur at comparable and smaller scales at these and lower altitudes, based on radar profiling and imaging cited above; examples include the KHI radar observations from the SBL into the MLT by Eaton et al. (1995), Geerts and Miao (2010), Fukao et al. (2011), Chau et al. (2020), and Grasmick and Geerts (2020), each of which reveals significant departures from spatially uniform KH billows. The evidence for T&K dynamics suggested by misaligned KH billows in tropospheric clouds reviewed by Thorpe (2002) is also compelling, but it did not reveal clear indications of T&K features at smaller scales.

Additional indirect evidence of potential small-scale KHI, and possible T&K dynamics, at very small scales is provided by high resolution in situ profiling employing instrumented balloons and small unmanned aircraft extending from the surface into the stratosphere enabling local assessments of temperature, horizontal winds, the temperature structure function C_T^2 and the energy dissipation rate ε (Coulman et al. 1995; Schneider et al. 2015; F16; Balsley et al. 2018; Doddi et al. 2022). These fields are complex and diverse, but often reveal enhanced C_T^2 , N^2 , and ε exhibiting potential responses to very small-scale KHI that resemble similar features in the F16 DNS modeling of MS GW environments. FW23 describes higher resolution results for the same initial fields and reveals such features to often be associated with KHI exhibiting T&K dynamics at very small scales and implied Re.

Further evidence for KHI T&K dynamics is seen in ocean acoustic profiling noted above. Importantly, while KHI roles in ocean mixing and induced large-scale overturning are anticipated even without potential T&K dynamics augmentations (e.g., Mashayek et al. 2015; Ferrari et al. 2016), their likely roles in the atmosphere are not fully appreciated. Hence, they remain largely unaccounted for in mixing and transport parameterizations above the SBL employed in global models. At higher altitudes, current schemes are based largely on idealized descriptions of GW breaking (Garcia et al. 2014; Liu 2021) requiring a "tuned" Pr ~ 2-4, based on idealized GW theory (Fritts and Dunkerton 1985; Coy and Fritts 1988; McIntyre 1989). We are not aware of any atmospheric parameterizations that attempt to account for turbulent mixing layers throughout the atmosphere due to KHI occurring at thin, strongly stratified, and sheared sheets, despite the extensive evidence for such sheets and widespread KHI, most likely including T&K dynamics, throughout the free atmosphere.

Key unknowns at present regarding KHI and their apparent widespread T&K dynamics in the atmosphere, oceans, and likely other stratified and sheared fluids include the following:

- 1) What are the driving dynamics, and how easily do they arise, in MS GW environments?
- 2) How do they vary with Ri, Re, and Pr?
- 3) Do T&K dynamics significantly enhance turbulence and mixing relative to their absence?

- 4) Are they suppressed or accelerated by background turbulence intensities?
- 5) Can they induce turbulence and mixing where it is not currently expected?
- 6) Are T&K dynamics competitive with GW breaking in driving mixing and transport?

Several of these questions will be answered, in part at least, by FW23, F23, and other papers in preparation. Others will require additional DNS and/or LES efforts, as T&K dynamics are influenced by diverse dynamics and the parameter space is extensive.

7. Conclusions

Initial DNS of KHI T&K dynamics by F22a and F22b described representative, but incomplete T&K dynamics driving turbulence transitions seen in early laboratory studies (Thorpe 1985, 1987) and suggested to be widespread in the atmosphere (Thorpe 2002). The most significant of these arise where two billows link to one or three billows link to two. Evidence for these additional T&K dynamics arise readily in MS GW environments, as seen at multiple sites in every PMC and OH airglow image sequence in Figs. 2–7, and others not shown. They are clearly widespread, and potentially ubiquitous, in the MLT and throughout the atmosphere. If so, KHI T&K dynamics may induce enhanced local turbulence and mixing relative to GW breaking, but their influences are neither recognized nor described in any parameterization at present.

To further understand, quantify, and assess the importance of KHI T&K dynamics, and their environmental dependencies, further studies need to include the following:

- additional idealized DNS employing different initial conditions, Ri, Re, and Pr, GW perturbations having varying frequencies, scales, amplitudes, and noise seeds that lead to additional, or enhanced, T&K dynamics, especially exhibiting misaligned KH billows along their axes;
- high-resolution LES describing KHI T&K dynamics in deeper domains configured to also describe superposed high-frequency GW and/or IGW initial conditions that more closely approximate the fields inferred to induce KHI T&K dynamics described here;
- idealized DNS exploration of the potential for KHI T&K dynamics to enable turbulence and mixing for smaller Re and larger Ri that would not arise in their absence; and
- 4) related studies in deep domains exploring the impacts of KHI T&K dynamics for potential enhanced GW radiation from shear layers, as proposed by Fritts (1984) and Chimonas and Grant (1984), and validated by Bühler et al. (1999) and Scinocca and Ford (2000).

The first three of these have been initiated; the fourth will require additional code upgrades to achieve the required resolution and computational efficiency.

Modeling efforts enabling improved parameterizations of KHI T&K dynamics will benefit greatly from their further quantification by simultaneous, common volume, imaging, and wind and/or temperature profiling in the MLT. Such observations would reveal the range of higher-frequency GW, IGW, and/or tidal environments and spatial scales enabling these dynamics in the MLT, and in dynamically similar environments at lower altitudes.

Acknowledgments. Observations and research by U.S. participants described here were performed under AFOSR Grant FA9550-18-0009, NSF Grants AGS-1647354, AGS-1651233, AGS-1758293, AGS-1829138, AGS-1829161, AGS-1911952, AGS-2032678, AGS-2131350, and AGS-2128443, and DARPA Grant HR00112120003 cited in GEMS. We thank the DoD HPCMP for computational resources that enabled the modeling results shown here. We also thank three anonymous reviewers and JAS editor Peter Bartello for many suggestions that significantly improved the paper. High-resolution movies showing the evolutions of various events are available as online supplemental material.

Data availability statement. PMC and OH airglow images in the various figures were extracted from the accompanying movies and the very large PMC Turbo imaging dataset is being uploaded to https://spdf.gsfc.nasa.gov/pub/data/aaa_balloons/pmc-turbo/l1_corrected-binned-images/. PFRR lidar data are available at http://boulder.gats-inc.com/~biff/page-3/page-7/index.html.

REFERENCES

- Andreassen, Ø., P. Ø. Hvidsten, D. C. Fritts, and S. Arendt, 1998: Vorticity dynamics in a breaking internal gravity wave. Part 1. Initial instability evolution. *J. Fluid Mech.*, 367, 27–46, https://doi.org/10.1017/S0022112098001645.
- Arendt, S., and D. C. Fritts, 1998: The instability of a vortex tube in a weak external shear and strain. *Phys. Fluids*, **10**, 530–532, https://doi.org/10.1063/1.869576.
- Baklanov, A. A., and Coauthors, 2011: The nature, theory, and modeling of atmospheric planetary boundary layers. *Bull. Amer. Meteor. Soc.*, **92**, 123–128, https://doi.org/10.1175/2010BAMS2797.1.
- Balsley, B. B., D. A. Lawrence, D. C. Fritts, L. Wang, K. Wan, and J. Werne, 2018: Fine structure, instabilities, and turbulence in the lower atmosphere: High-resolution in situ slant-path measurements with the DataHawk UAV and comparisons with numerical Modeling. *J. Atmos. Oceanic Technol.*, 35, 619–642, https://doi.org/10.1175/JTECH-D-16-0037.1.
- Baumgarten, G., and D. C. Fritts, 2014: Quantifying Kelvin-Helmholtz instability dynamics observed in noctilucent clouds: 1. Methods and observations. J. Geophys. Res. Atmos., 119, 9324–9337, https://doi.org/10.1002/2014JD021832.
- Blumen, W., R. Banta, S. P. Burns, D. C. Fritts, R. Newsom, G. S. Poulos, and J. Sun, 2001: Turbulence statistics of a Kelvin–Helmholtz billow event observed in the nighttime boundary layer during the Cooperative Atmosphere–Surface Exchange Study field program. *Dyn. Atmos. Oceans*, 34, 189– 204, https://doi.org/10.1016/S0377-0265(01)00067-7.
- Browning, K. A., and C. D. Watkins, 1970: Observations of clear air turbulence by high power radar. *Nature*, **227**, 260–263, https://doi.org/10.1038/227260a0.

- Bühler, O., M. E. McIntyre, and J. F. Scinocca, 1999: On shear-generated gravity waves that reach the mesosphere. Part I: Wave generation. *J. Atmos. Sci.*, **56**, 3749–3763, https://doi.org/10.1175/1520-0469(1999)056<3749:OSGGWT>2.0.CO;2.
- Caulfield, C. P., S. Yoshida, and W. R. Peltier, 1996: Secondary instability and three-dimensionalization in a laboratory accelerating shear layer with varying density differences. *Dyn. Atmos. Oceans*, 23, 125–138, https://doi.org/10.1016/ 0377-0265(95)00418-1.
- Chang, M.-H., S.-Y. Jheng, and R.-C. Lien, 2016: Trains of large Kelvin-Helmholtz billows observed in the Kuroshio above a seamount. *Geophys. Res. Lett.*, 43, 8654–8661, https://doi.org/ 10.1002/2016GL069462.
- Chau, J. L., J. M. Urco, V. Avsarkisov, J. P. Vierinen, R. Latteck, C. M. Hall, and M. Tsutsumi, 2020: Four-dimensional quantification of Kelvin-Helmholtz instabilities in the polar summer mesosphere using volumetric radar imaging. *Geophys. Res. Lett.*, 47, e2019GL086081, https://doi.org/10.1029/2019GL086081.
- Chimonas, G., and J. R. Grant, 1984: Shear excitation of gravity waves. Part II: Upscale scattering from Kelvin–Helmholtz waves. *J. Atmos. Sci.*, **41**, 2278–2288, https://doi.org/10.1175/1520-0469(1984)041<2278:SEOGWP>2.0.CO;2.
- Coulman, C. E., J. Vernin, and A. Fuchs, 1995: Optical seeing-mechanism of formation of thin turbulent laminae in the atmosphere. *Appl. Opt.*, 34, 5461–5474, https://doi.org/10.1364/AO.34.005461.
- Coy, L., and D. C. Fritts, 1988: Gravity wave heat fluxes: A Lagrangian approach. J. Atmos. Sci., 45, 1770–1780, https://doi.org/10.1175/1520-0469(1988)045<1770:GWLFAL>2.0.CO;2.
- De Silva, I. P. D., H. J. S. Fernando, F. Eaton, and D. Hebert, 1996: Evolution of Kelvin–Helmholtz billows in nature and laboratory. *Earth Planet. Sci. Lett.*, **143**, 217–231, https://doi.org/10.1016/0012-821X(96)00129-X.
- Doddi, A., D. Lawrence, D. Fritts, L. Wang, T. Lund, W. Brown, D. Zajic, and L. Kantha, 2022: Instabilities, Dynamics, and Energetics accompanying Atmospheric Layering (IDEAL): High-resolution in situ observations in and above the nocturnal boundary layer. Atmos. Meas. Tech., 15, 4023–4045, https://doi.org/10.5194/amt-15-4023-2022.
- Eaton, F., S. A. McLaughlin, and J. R. Hines, 1995: A new frequency-modulated continuous wave radar for studying planetary boundary layer morphology. *Radio Sci.*, 30, 75–88, https://doi.org/10.1029/94RS01937.
- Fernando, H. J. S., and J. C. Weil, 2010: Whither the stable boundary layer? *Bull. Amer. Meteor. Soc.*, 91, 1475–1484, https://doi.org/10.1175/2010BAMS2770.1.
- Ferrari, R., A. Mashayek, T. J. McDougall, M. Nikurashin, and J.-M. Campin, 2016: Turning ocean mixing upside down. J. Phys. Oceanogr., 46, 2239–2261, https://doi.org/10.1175/JPO-D-15-0244.1.
- Fritts, D. C., 1984: Shear excitation of atmospheric gravity waves. Part II. Nonlinear radiation from a free shear layer. *J. Atmos. Sci.*, **41**, 524–537, https://doi.org/10.1175/1520-0469(1984)041<0524:SEOAGW>2.0.CO;2.
- —, and T. J. Dunkerton, 1985: Fluxes of heat and constituents due to convectively unstable gravity waves. J. Atmos. Sci., 42, 549–556, https://doi.org/10.1175/1520-0469(1985)042<0549: FOHACD>2.0.CO;2.
- —, and P. K. Rastogi, 1985: Convective and dynamical instabilities due to gravity wave motions in the lower and middle atmosphere: Theory and observations. *Radio Sci.*, 20, 1247–1277, https://doi.org/10.1029/RS020i006p01247.

- —, and L. Wang, 2013: Gravity wave–fine structure interactions. Part II: Energy dissipation evolutions, statistics, and implications. *J. Atmos. Sci.*, **70**, 3735–3755, https://doi.org/10.1175/JAS-D-13-059.1.
- —, and —, 2023: Kelvin–Helmholtz instability "tube" and "knot" dynamics. Part II: KHI T&K dynamics in a multiscale gravity wave direct numerical simulation. *J. Atmos. Sci.*, 80, 2439–2457, https://doi.org/10.1175/JAS-D-22-0193.1.
- —, —, J. Werne, T. Lund, and K. Wan, 2009: Gravity wave instability dynamic at high Reynolds numbers. Part II: Turbulence evolution, structure, and anisotropy. *J. Atmos. Sci.*, 66, 1149–1171, https://doi.org/10.1175/2008JAS2727.1.
- —, and —, 2013: Gravity wave–fine structure interactions. Part I: Influences of fine structure form and orientation on flow evolution and instability. *J. Atmos. Sci.*, **70**, 3710–3734, https://doi.org/10.1175/JAS-D-13-055.1.
- —, G. Baumgarten, K. Wan, J. Werne, and T. S. Lund, 2014: Quantifying Kelvin-Helmholtz instability dynamics observed in noctilucent clouds: 2. Modeling and interpretation of observations. *J. Geophys. Res. Atmos.*, 119, 9359–9375, https:// doi.org/10.1002/2014JD021833.
- —, L. Wang, M. A. Geller, D. A. Lawrence, J. Werne, and B. B. Balsley, 2016: Numerical modeling of multi-scale dynamics at a high Reynolds number: Instabilities, turbulence, and an assessment of Ozmidov and Thorpe scales. *J. Atmos.* Sci., 73, 555–578, https://doi.org/10.1175/JAS-D-14-0343.1.
- —, and Coauthors, 2019: PMC Turbo: Studying gravity wave and instability dynamics in the summer mesosphere using polar mesospheric cloud imaging and profiling from a stratospheric balloon. *J. Geophys. Res. Atmos.*, **124**, 6423–6443, https://doi.org/10.1029/2019JD030298.
- —, S. A. Wieland, T. S. Lund, S. A. Thorpe, and J. H. Hecht, 2021: Kelvin-Helmholtz billow interactions and instabilities in the mesosphere over the Andes Lidar Observatory: 2. Modeling and interpretation. *J. Geophys. Res. Atmos.*, 125, e2020JD033412, https://doi.org/10.1029/2020JD033412.
- —, L. Wang, T. S. Lund, and S. A. Thorpe, 2022a: Multi-scale dynamics of Kelvin–Helmholtz instabilities. Part 1: Secondary instabilities and the dynamics of tubes and knots. *J. Fluid Mech.*, 941, A30, https://doi.org/10.1017/jfm.2021.1085.
- —, —, S. A. Thorpe, and T. S. Lund, 2022b: Multi-scale dynamics of Kelvin–Helmholtz instabilities. Part 2: Energy dissipation rates, evolutions, and statistics. *J. Fluid Mech.*, 941, A31, https://doi.org/10.1017/jfm.2021.1086.
- —, T. S. Lund, S. A. Thorpe, C. B. Kjellstrand, B. Kaifler, and N. Kaifler, 2022c: Multi-scale Kelvin-Helmholtz instability dynamics observed by PMC Turbo on 12 July 2018: 2. DNS modeling of KHI dynamics and PMC responses. *J. Geophys. Res. Atmos.*, 127, e2021JD035834, https://doi.org/10.1029/2021JD035834.
- Fukao, S., H. Luce, T. Mega, and M. K. Yamamoto, 2011: Extensive studies of large-amplitude Kelvin–Helmholtz billows in the lower atmosphere with VHF middle and upper atmosphere radar. *Quart. J. Roy. Meteor. Soc.*, **137**, 1019–1041, https://doi.org/10.1002/qj.807.
- Garcia, R. R., M. Lopez-Puertas, B. Funke, D. R. Marsh, D. E. Kinnison, A. K. Smith, and F. Gonzalez-Galindo, 2014: On the distribution of CO₂ and CO in the mesosphere and lower thermosphere. *J. Geophys. Res. Atmos.*, 119, 5700–5718, https://doi.org/10.1002/2013JD021208.
- Geerts, B., and Q. Miao, 2010: Vertically pointing airborne Doppler radar observations of Kelvin–Helmholtz billows. Mon. Wea. Rev., 138, 982–986, https://doi.org/10.1175/2009MWR3212.1.

- Geyer, W. R., A. C. Lavery, M. E. Scully, and J. H. Trow-bridge, 2010: Mixing by shear instability at high Reynolds number. *Geophys. Res. Lett.*, 37, L22607, https://doi.org/10.1029/2010GL045272.
- Gossard, E. E., 1990: Radar research on the atmospheric boundary layer. *Radar in Meteorology*, D. Atlas, Ed., Amer. Meteor. Soc., 477–527.
- Grasmick, C., and B. Geerts, 2020: Detailed dual-Doppler structure of Kelvin–Helmholtz waves from an airborne profiling radar over complex terrain. Part I: Dynamic structure. *J. Atmos. Sci.*, 77, 1761–1782, https://doi.org/10.1175/JAS-D-19-0108.1.
- Hecht, J. H., A. Z. Liu, R. L. Walterscheid, and R. J. Rudy, 2005: Maui Mesosphere and Lower Thermosphere (Maui MALT) observations of the evolution of Kelvin-Helmholtz billows formed near 86 km altitude. J. Geophys. Res., 110, D09S10, https://doi.org/10.1029/2003JD003908.
- —, and Coauthors, 2014: The life cycle of instability features measured from the Andes Lidar Observatory over Cerro Pachon on 24 March 2012. *J. Geophys. Res. Atmos.*, 119, 8872– 8898, https://doi.org/10.1002/2014JD021726.
- —, and Coauthors, 2018: Observations of the breakdown of mountain waves over the Andes Lidar Observatory at Cerro Pachon on 8/9 July 2012. *J. Geophys. Res. Atmos.*, **123**, 276– 299, https://doi.org/10.1002/2017JD027303.
- —, D. C. Fritts, L. J. Gelinas, R. J. Rudy, R. L. Walterscheid, and A. Z. Liu, 2021: Kelvin-Helmholtz billow interactions and instabilities in the mesosphere over the Andes Lidar Observatory: 1. Observations. J. Geophys. Res. Atmos., 126, e2020JD033414, https://doi.org/10.1029/2020JD033414.
- Holt, J. T., 1998: Experiments on Kelvin-Helmholtz billows influenced by boundaries. *Geophys. Astrophys. Fluid Dyn.*, 89, 205–233, https://doi.org/10.1080/03091929808203686.
- Hysell, D. L., E. Nossa, M. F. Larsen, M. Munro, S. Smith, M. P. Sulzer, and S. A. Gonzalez, 2012: Dynamic instability in the lower thermosphere inferred from irregular sporadic *E* layers. *J. Geophys. Res.*, 117, A08305, https://doi.org/10.1029/2012JA017910.
- Jeong, J., and F. Hussain, 1995: On the identification of a vortex. J. Fluid Mech., 285, 69–94, https://doi.org/10.1017/S0022112095000462.
- Kaifler, B., and N. Kaifler, 2021: A Compact Rayleigh Autonomous Lidar (CORAL) for the middle atmosphere. Atmos. Meas. Tech., 14, 1715–1732, https://doi.org/10.5194/amt-14-1715-2021.
- —, D. Rempel, P. Roßi, H. C. Büdenbender, N. Kaifler, and V. Baturkin, 2020: A technical description of the Balloon Lidar Experiment (BOLIDE). *Atmos. Meas. Tech.*, 13, 5681– 5695, https://doi.org/10.5194/amt-13-5681-2020.
- Kaifler, N., B. Kaifler, H. Wilms, M. Rapp, G. Stober, and C. Jacobi, 2018: Mesospheric temperature during the extreme mid-latitude noctilucent cloud event on 18/19 July 2016. *J. Geophys. Res. Atmos.*, 123, 13775–13789, https://doi.org/10.1029/2018JD029717.
- Kjellstrand, C. B., and Coauthors, 2020: The PMC Turbo balloon mission to measure gravity waves and turbulence in polar mesospheric clouds: Camera, telemetry, and software performance. *Earth Space Sci.*, 7, e2020EA001238, https://doi.org/10.1029/ 2020EA001238.
- —, and Coauthors, 2022: Multi-scale Kelvin-Helmholtz instability dynamics observed by PMC-Turbo on 12 July 2018: 1. Secondary instabilities and billow interactions. *J. Geophys. Res. Atmos.*, 127, e2021JD036232, https://doi.org/10.1029/2021JD036232.

- Larsen, M. F., 2002: Winds and shears in the mesosphere and lower thermosphere: Results from four decades of chemical release wind measurements. J. Geophys. Res., 107, 1215, https://doi.org/10.1029/2001JA000218.
- Lelong, M.-P., and T. J. Dunkerton, 1998: Inertia–gravity wave breaking in three dimensions. Part 1. Convectively stable waves. J. Atmos. Sci., 55, 2473–2488, https://doi.org/10.1175/ 1520-0469(1998)055<2473:IGWBIT>2.0.CO;2.
- Li, J., B. P. Williams, J. H. Alspach, and R. L. Collins, 2020: Sodium Resonance Wind-Temperature Lidar at PFRR: Initial observations and performance. *Atmosphere*, 11, 98, https:// doi.org/10.3390/atmos11010098.
- Liu, H.-L., 2021: Effective vertical diffusion by atmospheric gravity waves. *Geophys. Res. Lett.*, 48, e2020GL091474, https://doi.org/10.1029/2020GL091474.
- Luce, H., G. Hassenpflug, M. Yamamoto, M. Crochet, and S. Fukao, 2007: Range-imaging observations of cumulus convection and Kelvin-Helmholtz instabilities with the MU radar. *Radio Sci.*, 42, RS1005, https://doi.org/10.1029/2005RS003439.
- —, —, S. Fukao, and K. Sato, 2008: High-resolution observations with MU radar of a KH instability triggered by an inertia–gravity wave in the upper part of a jet stream. *J. Atmos. Sci.*, **65**, 1711–1718, https://doi.org/10.1175/2007JAS2346.1.
- —, L. Kantha, M. Yabuki, and H. Hashiguchi, 2018: Atmospheric Kelvin–Helmholtz billows captured by the MU radar, lidars and a fish-eye camera. *Earth Planets Space*, 70, 162, https://doi.org/10.1186/s40623-018-0935-0.
- Ludlam, F. H., 1967: Billow clouds and their relation to clear air turbulence. Quart. J. Roy. Meteor. Soc., 93, 419–435, https:// doi.org/10.1002/qj.49709339803.
- Mashayek, A., and W. R. Peltier, 2013: Shear-induced mixing in geophysical flows: Does the route to turbulence matter to its efficiency? J. Fluid Mech., 725, 216–261, https://doi.org/10. 1017/jfm.2013.176.
- —, R. Ferrari, M. Nikurashin, and W. R. Peltier, 2015: Influence of enhanced abyssal diapycnal mixing on ocean stratification and overturning circulation. *J. Phys. Oceanogr.*, 45, 2580–2597, https://doi.org/10.1175/JPO-D-15-0039.1.
- McIntyre, M. E., 1989: On dynamics and transport near the polar mesopause in summer. J. Geophys. Res., 94, 14617–14628, https://doi.org/10.1029/JD094iD12p14617.
- Mesquita, R. L. A., M. F. Larsen, I. Azeem, M. H. Stevens, B. P. Williams, R. L. Collins, and J. Li, 2020: In situ observations of neutral shear instability in the statically stable high-latitude mesosphere and lower thermosphere during quiet geomagnetic conditions. J. Geophys. Res. Space Phys., 125, e2020JA027972, https://doi.org/10.1029/2020JA027972.
- Moum, J. N., D. M. Farmer, W. D. Smyth, L. Armi, and S. Vagle, 2003: Structure and generation of turbulence at interfaces strained by internal solitary waves propagating shoreward over the continental shelf. J. Phys. Oceanogr., 33, 2093–2112, https://doi.org/10.1175/1520-0485(2003)033<2093:SAGOTA> 2.0.CO;2.
- Pautet, P.-D., M. J. Taylor, W. R. Pendleton, Y. Zhao, T. Yuan, R. Esplin, and D. McLain, 2014: Advanced Mesospheric Temperature Mapper for high-latitude airglow studies. *Appl. Opt.*, 53, 5934–5943, https://doi.org/10.1364/AO.53.005934.
- Pfrommer, T., P. Hickson, and C.-Y. She, 2009: A large-aperture sodium fluorescence lidar with very high resolution for mesopause dynamics and adaptive optics studies. *Geophys. Res. Lett.*, **36**, L15831, https://doi.org/10.1029/2009GL038802.
- Rapp, M., B. Strelnikov, A. Müllemann, F.-J. Lübken, and D. C. Fritts, 2004: Turbulence measurements and implications for

- gravity wave dissipation during the MaCWAVE/MIDAS summer rocket program. *Geophys. Res. Lett.*, **31**, L24S07, https://doi.org/10.1029/2003GL019325.
- Reichert, R. B., B. Kaifler, N. Kaifler, A. Dörnbrack, M. Rapp, and J. L. Hormaechea, 2021: High-cadence lidar observations of middle atmospheric temperature and gravity waves at the southern Andes hot spot. J. Geophys. Res. Atmos., 126, e2021JD034683, https://doi.org/10.1029/2021JD034683.
- Schäfer, B., G. Baumgarten, and J. Fiedler, 2020: Small-scale structures in noctilucent clouds observed by lidar. J. Atmos. Sol.-Terr. Phys., 208, 105384, https://doi.org/10.1016/j.jastp.2020.105384.
- Schneider, A., M. Gerding, and F.-J. Lübken, 2015: Comparing turbulent parameters obtained from LITOS and radiosonde measurements. *Atmos. Chem. Phys.*, 15, 2159–2166, https:// doi.org/10.5194/acp-15-2159-2015.
- Schowalter, D. G., C. W. Van Atta, and J. C. Lasheras, 1994: A study of streamwise vortex structure in a stratified shear layer. J. Fluid Mech., 281, 247–291, https://doi.org/10.1017/ S0022112094003101.
- Scinocca, J. F., and R. Ford, 2000: The nonlinear forcing of large-scale internal gravity waves by stratified shear instability. *J. Atmos. Sci.*, **57**, 653–672, https://doi.org/10.1175/1520-0469(2000)057<0653:TNFOLS>2.0.CO:2.
- Scorer, R. S., 1951: Billow clouds. *Quart. J. Roy. Meteor. Soc.*, **77**, 235–240, https://doi.org/10.1002/qj.49707733208.
- ——, 1969: Billow mechanics. *Radio Sci.*, 4, 1299–1308, https://doi. org/10.1029/RS004i012p01299.
- —, and H. Wexler, 1963: A Colour Guide to Clouds. Pergamon Press, 70 pp.
- She, C. Y., J. D. Vance, B. P. Williams, D. A. Krueger, H. Moosmuller, D. Gibson-Wilde, and D. C. Fritts, 2002: Lidar studies of atmospheric dynamics near polar mesopause. *Eos, Trans. Amer. Geophys. Union*, 83, 289–293, https://doi.org/10.1029/2002EO000206.
- Taylor, M. J., and Coauthors, 2019: Large-amplitude mountain waves in the mesosphere observed on 21 June 2014 during DEEP-WAVE: 1. Wave development, scales, momentum fluxes, and environmental sensitivity. J. Geophys. Res. Atmos., 124, 10364– 10384, https://doi.org/10.1029/2019JD030932.
- Thomson, S. W., 1880: Vibrations of a columnar vortex. *Philos. Mag.*, **10**, 155–168, https://doi.org/10.1080/14786448008626912.

- Thorpe, S. A., 1973a: Experiments on instability and turbulence in a stratified shear flow. *J. Fluid Mech.*, **61**, 731–751, https://doi.org/10.1017/S0022112073000911.
- —, 1973b: Turbulence in stably stratified fluids: A review of laboratory experiments. *Bound.-Layer Meteor.*, 5, 95–119, https:// doi.org/10.1007/BF02188314.
- —, 1985: Laboratory observations of secondary structures in Kelvin-Helmhoitz billows and consequences for ocean mixing. *Geophys. Astrophys. Fluid Dyn.*, 34, 175–199, https://doi. org/10.1080/03091928508245442.
- —, 1987: Transitional phenomena and the development of turbulence in stratified fluids: A review. J. Geophys. Res., 92, 5231–5248, https://doi.org/10.1029/JC092iC05p05231.
- —, 2002: The axial coherence of Kelvin–Helmholtz billows. Quart. J. Roy. Meteor. Soc., 128, 1529–1542, https://doi.org/10. 1002/qj.200212858307.
- Tu, J., D. Fan, Q. Lian, Z. Liu, W. Liu, A. Kaminski, and W. Smyth, 2020: Acoustic observations of Kelvin-Helmholtz billows on an estuarine lutocline. *J. Geophys. Res. Oceans*, 125, e2019JC015383, https://doi.org/10.1029/2019JC015383.
- Watanabe, T., J. J. Riley, K. Nagata, K. Matsuda, and R. Onishi, 2019: Hairpin vortices and highly elongated flow structures in a stably stratified shear layer. J. Fluid Mech., 878, 37–71, https://doi.org/10.1017/jfm.2019.577.
- Williams, B. P., and Coauthors, 2004: Gravity waves in the Arctic mesosphere during the MaCWAVE/MIDAS summer rocket program. *Geophys. Res. Lett.*, 31, L24S05, https://doi.org/10. 1029/2004GL020049.
- —, D. C. Fritts, C. Y. She, and R. A. Goldberg, 2006: Gravity wave propagation through a large semidiurnal tide and instabilities in the mesosphere and lower thermosphere during the winter 2003 MaCWAVE rocket campaign. *Ann. Geophys.*, 24, 1199–1208, https://doi.org/10.5194/angeo-24-1199-2006.
- Witt, G., 1962: Height, structure and displacements of noctilucent clouds. *Tellus*, **14**, 1–18, https://doi.org/10.3402/tellusa.v14i1.
- Woods, J. D., 1968: Wave-induced shear instability in the summer thermocline. *J. Fluid Mech.*, **32**, 791–800, https://doi.org/10. 1017/S0022112068001035.
- ——, and R. L. Wiley, 1972: Billow turbulence and ocean microstructure. *Deep-Sea Res.*, **19**, 87–121, https://doi.org/10.1016/ 0011-7471(72)90043-5.